

# FE Modelling of Two Femur Fixation Implants

---

*Thesis Report*

**Ali S. Arsiwala & Vatsal Shukla**

Examiner : Joakim Holmberg

Supervisor : Jonas Stålhand

External Supervisor : Daphne Wezenberg

## Upphovsrätt

Detta dokument hålls tillgängligt på Internet - eller dess framtida ersättare - under 25 år från publiceringsdatum under förutsättning att inga extraordinära omständigheter uppstår.

Tillgång till dokumentet innebär tillstånd för var och en att läsa, ladda ner, skriva ut enstaka kopior för enskilt bruk och att använda det oförändrat för ickekommersiell forskning och för undervisning. Överföring av upphovsrätten vid en senare tidpunkt kan inte upphäva detta tillstånd. All annan användning av dokumentet kräver upphovsmannens medgivande. För att garantera äktheten, säkerheten och tillgängligheten finns lösningar av teknisk och administrativ art.

Upphovsmannens ideella rätt innefattar rätt att bli nämnd som upphovsman i den omfattning som god sed kräver vid användning av dokumentet på ovan beskrivna sätt samt skydd mot att dokumentet ändras eller presenteras i sådan form eller i sådant sammanhang som är kränkande för upphovsmannens litterära eller konstnärliga anseende eller egenart.

För ytterligare information om Linköping University Electronic Press se förlagets hemsida <http://www.ep.liu.se/>.

## Copyright

The publishers will keep this document online on the Internet - or its possible replacement - for a period of 25 years starting from the date of publication barring exceptional circumstances.

The online availability of the document implies permanent permission for anyone to read, to download, or to print out single copies for his/hers own use and to use it unchanged for non-commercial research and educational purpose. Subsequent transfers of copyright cannot revoke this permission. All other uses of the document are conditional upon the consent of the copyright owner. The publisher has taken technical and administrative measures to assure authenticity, security and accessibility.

According to intellectual property law the author has the right to be mentioned when his/her work is accessed as described above and to be protected against infringement.

For additional information about the Linköping University Electronic Press and its procedures for publication and for assurance of document integrity, please refer to its www home page: <http://www.ep.liu.se/>.

## Abstract

In the pool of women over the age of 50, the likeliness of an atypical fracture increases drastically, partly due to osteoporosis. With a pre-existing implant in the femur bone, inserted due to a prior atypical fracture, treating a later femoral neck fracture is complex and risky. Currently, a fractured femoral diaphysis is treated using an intermedullary nail which is fixed to the femur bone either through the femoral neck (Recon locking method) or through the lesser trochanter (Antegrade locking method). In a study conducted by Bögl *et.al.* *JBJS* 102.17 (2020), pp. 1486-1494, it is found that the fixation of the intermedullary nail through the femoral neck reduces the risk of future femoral neck fractures. The study also states that more than 50% of the patients with atypical femoral fractures related to biophosphonate treatment for osteoporosis (within the study sub population) were treated with the Antegrade locking implant. There does not exist much literature that reasons as to how one locking method is showing lesser risk of re-operation as compared to the other. The purpose of this study is to look into the effects these two implants have on the femur bone using the Finite Element Analysis (FEA). The study presented is aimed at comparing the results of the finite element analysis for the Recon implant model (Recon model) and Antegrade implant model (Antegrade model). The femur model without the implants (native bone model) is used to verify material behavior, while the other two are used for the comparison to study the stress-strain distribution, primarily in the neck region.

This is a patient specific study, hence the femur bone model is generated using patient Computed Tomography (CT) scans. The bone model was assigned a heterogeneous isotropic material property derived from patient CT data. The finite element (FE) model of the bone was meshed using Hypermesh. The peak loading condition including the muscle forces were applied on the native bone model along with the Recon and the Antegrade model. While the loading conditions during normal walking cycle were only applied to the Recon and the Antegrade model to compare the impacts of the two implant types. Both loading conditions were simulated by fixing the distal condyle region of the bone.

The analysis results show that the Antegrade implant experiences much higher stresses and strains in the neck region as compared to Recon implant. Also, the presence of the intermedullary nail through the femur diaphysis helps to distribute the stresses and strains in the anterior distal diaphysis region of the bone. For the case of no implants, the model showed strains and stresses in the lateral distal region of femoral diaphysis.

# Acknowledgments

This thesis was conducted at the Division of Solid Mechanics, Linköping University, in collaboration with the Orthopedic Department at University Hospital, Linköping.

We would like to thank our supervisors Prof. Jonas Stålhand and Dr. Daphne Wezenberg for their constant patience, support and invaluable guidance throughout the course of the project. We would like to thank our examiner Prof. Joakim Holmberg for his open communication, guidance and making sure the required resources were allocated for the fruition of the thesis.

We would also like to give a special thanks to Dr. Jörg Schilcher, Mr. Jordi Loureiro and Dr. Anna Gustafsson for sharing their expertise in various topics and pointing us in the right direction.

Finally, we would also like to acknowledge the support of our parents and families, more so due to the uniqueness of the external circumstances that this thesis was carried out in.

**Vatsal Shukla**

**Ali S. Arsiwala**

October 7, 2021

# Contents

<b>Abstract</b>	<b>iii</b>
<b>Acknowledgments</b>	<b>iv</b>
<b>Contents</b>	<b>v</b>
<b>List of Figures</b>	<b>vi</b>
<b>List of Tables</b>	<b>viii</b>
<b>1 Introduction</b>	<b>1</b>
1.1 Problem Formulation . . . . .	2
1.2 Aim . . . . .	2
1.3 Research questions . . . . .	2
<b>2 Theory</b>	<b>3</b>
2.1 Femur Bone . . . . .	3
2.2 Image Segmentation: ITK-Snap . . . . .	5
2.3 Material Modelling . . . . .	6
<b>3 Method</b>	<b>8</b>
3.1 Image segmentation . . . . .	8
3.2 CAD design of Implants . . . . .	11
3.3 Meshing . . . . .	12
3.4 Material Mapping . . . . .	15
3.5 FE Model Setup . . . . .	16
<b>4 Results</b>	<b>21</b>
4.1 Bonemat . . . . .	21
4.2 Finite Element Analysis. . . . .	22
<b>5 Discussion</b>	<b>32</b>
5.1 Results . . . . .	32
5.2 Method . . . . .	33
5.3 Limitations and future scope . . . . .	34
<b>6 Conclusion</b>	<b>36</b>
<b>I Appendix</b>	<b>37</b>
<b>Bibliography</b>	<b>39</b>

# List of Figures

1.1	(a) Shaft fracture of femur bone (b) Fixing the intermedullar nail through the neck (Recon locking) (c) Fixing the intermedullar nail through the lesser trochanter (Antegrade locking) . . . . .	1
2.1	Bone Anatomy . . . . .	3
2.2	Directional view nomenclature . . . . .	4
2.3	Cortical Bone Structure . . . . .	4
2.4	Trabecular bone biopsy showing the lattice-like structure . . . . .	5
3.1	(a) Original DICOM image; (b) Contrast adjusted DICOM image . . . . .	8
3.2	Selection of ROI; the red box depicts the selection . . . . .	9
3.3	(a) and (b) depict label classification in two different slices of the image . . . . .	9
3.4	(a) and (b) depict active contours placed in two different slices of the image . . . . .	10
3.5	Final model obtained from ITK Snap . . . . .	10
3.6	(a) 5.0 mm fully threaded locking screw (b) 6.5mm cannulated lag screw (C) Description of the Recon and Antegrade nails . . . . .	11
3.7	(a)Recon fixation assembly - front view and (b)Recon fixation assembly - side view, with locking screws(bottom), cannulated screws(top) and the bone; (c) Antegrade fixation assembly - front view and (d) Antegrade fixation assembly - side view, with locking screws (top and bottom) and the bone . . . . .	12
3.8	The figure shows the initial to final mesh transformation;(a)Initial mesh with 609,232 faces and 304,620 vertices;(b) After making the mesh coarse, 45,876 faces and 22,938 vertices; (c) Making the mesh more coarse and smoothing it, 15074 faces and 7539 vertices . . . . .	13
3.9	The yellow surfaces represent shared surfaces between two parts . . . . .	14
3.10	(a) Bone without implants; (b)Bone with Recon locking; (c)Bone with Antegrade locking . . . . .	14
3.11	Each section view correlated to the colored line; Green mesh : Bone ; Red mesh : Implant . . . . .	15
3.12	Bonemat configuration file, showing inputs for the constants . . . . .	16
3.13	Selected surfaces for constraint . . . . .	17
3.14	MPC tie constraint between RP and node-set for hip joint load . . . . .	17
3.15	x, y, z = axes of femur coordinate system. x = parallel to posterior contour of condyles. P1 = intersection of neck axis and femoral midline. P2 = middle of intercondylar notch. z = straight femur axis between P1 and P2. Force components $F_x, F_y$ and $F_z$ act in directions x, y and z. Moment components $M_x, M_y$ and $M_z$ turn clockwise around x, y and z. The implant is turned clockwise by angles $\alpha_z, \alpha_y$ and $\alpha_x$ around the femur axes z, y and x. $\alpha_z$ = anteversion of neck (negative). $x', y', z'$ = axes of implant. $x_n, y_n, z_n$ = coordinate system at distal end of implant neck. $x_s, y_s, z_s$ = coordinate system of stem 80 mm below head centre . . . . .	18
3.16	Force components of the applied hip load, in [x y z] coordinate system of femur model . . . . .	19
3.17	Placement of hip contact along with the muscle groups . . . . .	19

3.18	Fixed support BC at the femoral condyle surface in the distal region of the femur .	20
4.1	Mapped Young’s modulus on the no-implant bone model . . . . .	21
4.2	Position and orientation of the section view planes . . . . .	22
4.3	Maximum principal strains in the neck region . . . . .	23
4.4	Maximum principal stress in the neck region . . . . .	24
4.5	Max. principal strain across the shaft for Native bone . . . . .	25
4.6	Max. principal strain across the shaft for bone with Recon implant . . . . .	25
4.7	Max. principal strain across the shaft for bone with Antegrade implant . . . . .	26
4.8	Max. principal stress across the shaft for Native bone . . . . .	26
4.9	Max. principal stress across the shaft for bone with Recon implant . . . . .	27
4.10	Max. principal stress across the shaft for bone with Antegrade implant . . . . .	27
4.11	Stress and strain across femur neck for loading without muscle forces . . . . .	28
4.12	Max. principal strain across the shaft for bone with Recon implant . . . . .	29
4.13	Max. principal strain across the shaft for bone with Antegrade implant . . . . .	29
4.14	Max. principal stress across the shaft for bone with Recon implant . . . . .	30
4.15	Max. principal stress across the shaft for bone with Antegrade implant . . . . .	30
I.1	Image slice used to calculate HU average . . . . .	37

# List of Tables

2.1	Calibration phantom material details . . . . .	7
3.1	Mesh details . . . . .	14
3.2	Load values of hip contact and three major muscle groups during the stance phase of the load cycle . . . . .	20
4.1	List of different material sets. . . . .	21
I.1	Calculated HU values. . . . .	38

# 1 Introduction

Fractures of hip and adjoining regions can be classed as a common occurrence over a certain age [1], especially in the Scandinavian countries, which have the highest number of cases of hip and femoral neck fractures, with majority of patients being women [2, 3]. For women over the age of 50, the likeliness of an atypical fracture is increased due to various risk factors such as ethnicity, osteoporosis, impaired balance, and also due to reduced lower-extremity functions and reduced mobility in the joints [3]. Due to the condition of osteoporosis, which in itself is common, the chances of femoral neck fracture is increased in later years. When the femoral diaphysis (shaft) is fractured, it is treated by passing an intermedullary nail through the intermedullary canal of the femur. This nail is then secured in place using either the Recon locking or the Antegrade locking method. The figures below (1.1b and 1.1c) show the two locking types. The Recon locking (Recon implant) has the Recon nail passing through the femur neck while the Antegrade locking (Antegrade implant) has the nail passing through the greater and the lesser trochanter. The treatment for neck fractures on a bone with a pre-existing implant of the intermedullary nail due to a shaft fracture is a complex, risky process with high chances of infections and is relatively time consuming.

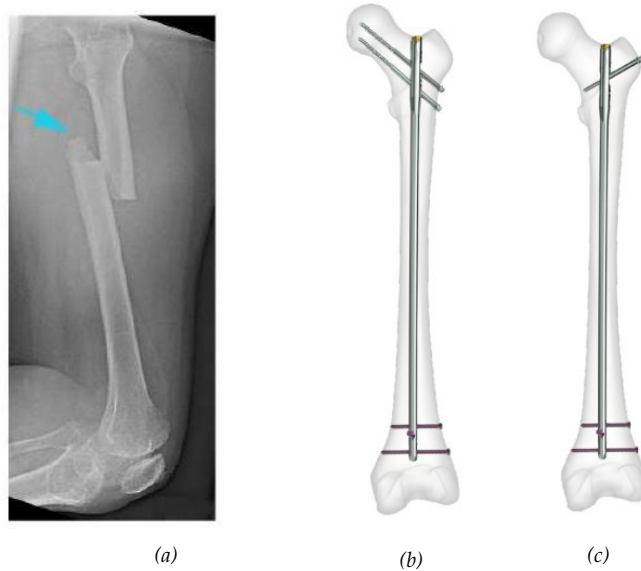


Figure 1.1: (a) Shaft fracture of femur bone (b) Fixing the intermedullary nail through the neck (Recon locking) (c) Fixing the intermedullary nail through the lesser trochanter (Antegrade locking) [4].

## 1.1 Problem Formulation

In a study conducted by Bögl *et.al.* [3] the re-operation frequency for patients with Recon implants is compared against patients with Antegrade implants. The study also states that more than 50% of the patients with atypical femoral fractures related to biophosphonate treatment for osteoporosis (within the study sub population) were treated with the Antegrade locking implant [3]. Bögl concluded that the intermedullary nail, when fixated through the neck (Recon locking method), showed less cases of re-operations as compared to the fixation through the lesser trochanter (Antegrade locking method). Also, the Recon locking mechanism showed lower risk of proximal peri-implant fractures, which are the fractures caused near the implants. Furthermore, the paper discusses the lack of literature on reasons for increased use of one implant type over the other. This, we believe, merits further investigation to understand such an occurrence.

## 1.2 Aim

The aim of this thesis was to perform a patient-specific study using the Finite Element Method (FEM) to understand the flow of stresses and strains through the femur bone with two types of the implants. This may improve the understanding of the reasons behind the findings of Bögl *et.al.* [3]. If we know how the implants affects the bone, maybe future treatments could have a calculated response to what locking method is best for the situation. Hence a better understanding of the mechanisms associated with nail fixation is desirable. Keeping this in mind, the following objectives were defined:

- Find a method to create a femur model from the provided patient Computed Tomography (CT) scans.
- Assign appropriate material property to the bone, derived from patient data.
- Compare the stress and strain contours obtained from Finite Element Analysis (FEA) results for the Recon implant model and Antegrade implant model.

## 1.3 Research questions

In the attempt to postulate the reasons behind the reduced risks of Recon implant over Antegrade implant, following research questions have been formulated:

- How can the femur bone be modelled from the patient CT-Scans?
- How can the material property of the patient's bone be assigned to the model?
- How will the FE model be setup, along with the boundary conditions to replicate a realistic scenario?
- How can the assigned material property be verified?
- What quantities, from FEA results are to be compared to derive the conclusion?

## 2 Theory

### 2.1 Femur Bone

Human body consists of 206 bones. The femur bone is located in the thigh and is the longest bone in the body. Femur is basically divided into two regions: *distal* region and *proximal* region.

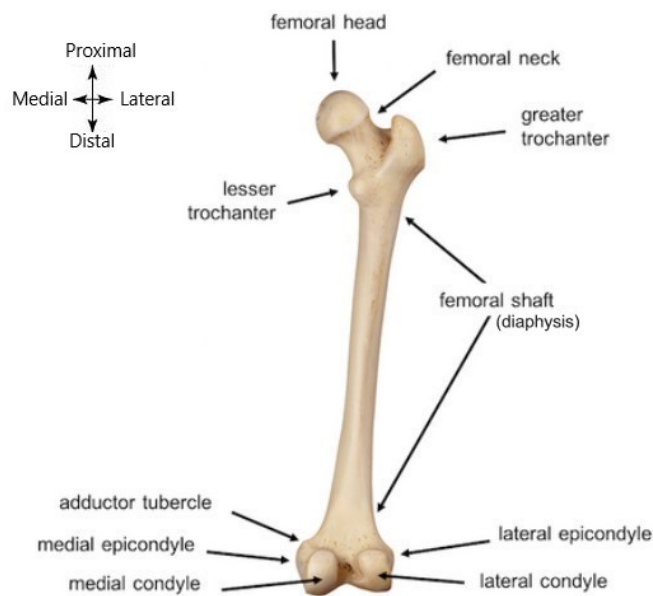


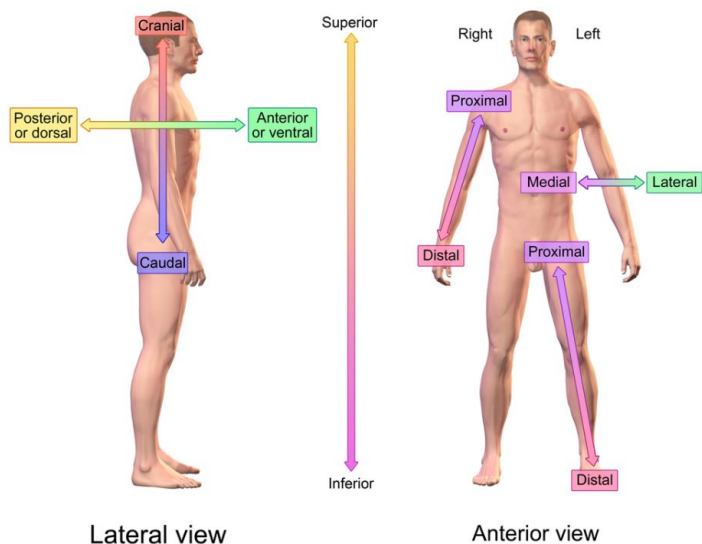
Figure 2.1: Bone Anatomy [5]

The *proximal* region is close to the pelvic bone forming the hip joint and the *distal* region is near the knee joint. The *proximal* region consists of femoral head, neck, greater trochanter and lesser trochanter. The diaphysis (shaft) of the femur is the central long section of the femur. The *distal* region consists of adductor tubercle, epicondyle and condyle.

Figure 2.2 gives the nomenclature of the views and positional references used in the thesis.

### Bone Material

The skeletal system provides the framework for the body. It consists of bone and cartilages which together absorb the forces exerted on the body and protect organs, among other functionalities [7]. Due to this the skeletal system has evolved leading to bones that can be modelled as rigid or elastic depending on magnitude and direction of the forces being applied. On the macroscopic level, human bone consists of two types of bone material: cortical and trabecular.



Directional References

Figure 2.2: Directional view nomenclature [6]

Cortical bone is the dense hard bone that is generally found as an outer layer. This is the stiffer of the two bones having a higher Young’s modulus in the range 11.4-21.6 GPa [8]. It consists of longitudinal oriented cylinders known as the Haversians system. These systems house the nerves and the blood vessels [7] (figure 2.3).

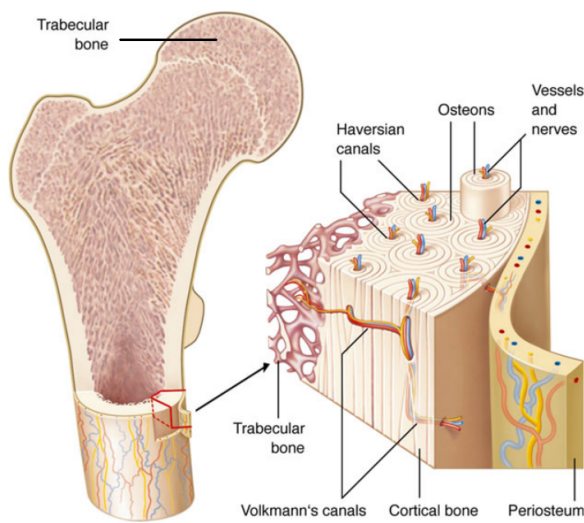


Figure 2.3: Cortical Bone Structure [7]

The trabecular bone is soft, porous and provides the bone with the much required elasticity. The general stiffness of the trabecular bone ranges from 0.2-1.1 GPa [8]. This bone material is generally found in the distal and the proximal regions of long bones (e.g. femur, tibia), in flat bones (e.g. ilium) and in cuboidal bones (e.g. vertebrae) [9]. Figure2.3 illustrates the trabecular bone in the femoral head. Figure 2.4 shows the trabecular bone structure as seen in a bone biopsy.



Figure 2.4: Trabecular bone biopsy showing the lattice-like structure [7]

A bone *in vivo* comprises of not only the hard bony material but also blood, water and other fluids. This changes the overall density of the bone as a whole. In a patient specific study where the bone sample is a part of the living patient, multiple densities of a particular bone need to be considered to be able to effectively derive its material properties. The densities required for this thesis have been listed below along with their brief descriptions:

- Apparent Bone Density ( $\rho_{app}$ ): Weight of the sample divided by the volume of the sample. Here the sample is fresh.
- Bone Ash Density ( $\rho_{ash}$ ): Mineral weight of the sample divided by the volume of the sample. the mineral weight is determined by burning the sample to remove water and weight the ashes remaining.
- Radiological Density ( $\rho_{qct}$ ): The known density of a material that provides the same X-ray attenuation to the sample being scanned.

These densities were used to find the material properties of the patient bone. The relation between them and to the material stiffness will be discussed in later sections.

## 2.2 Image Segmentation: ITK-Snap

The process of active contour segmentation can be described as navigating layer by layer through a 3-D image to pin-point the region of interest that are required to be converted into a 3-D model. This can be done using a segmentation algorithm that allows the user to define parameters that describe the region that the user wishes to segment, known as automatic segmentation method. Alternatively, the user can manually perform the process by navigating through each slice of the 3-D imaging and selecting the regions themselves. The CT image is a greyscale 3-D image consisting of various components (bone, muscle tissues) separated by the voxel (smallest constituent of a 3-D image; synonymous to pixel in a 2-D image) intensity in that area. The segmentation process was carried out using the software ITK-Snap [10] (For further references see [www.itksnap.org](http://www.itksnap.org)). The interface of ITK-Snap allows the user to access 3-D medical images (Digital Imaging and Communications in Medicine (DICOM) and Neuroimaging Informatics Technology Initiative (NIFTI) formats accepted) and perform automatic and semi-automatic segmentation to obtain a 3-D model of a specific component of the image. The first step of the segmentation process is extracting the region of interest (ROI) from main DICOM image. ITK-Snap allows the user to manipulate the parameters of the image such as contrast, color scale and threshold parameters to aid the identification of the constituents while filtering out unwanted details. The automatic segmentation algorithm allows the user to train the algorithm to identify components of the image by manually assigning labels (classifiers) to regions with differing intensities. The next step is to manually place evolving contours on the image. These contours can be described as closed surfaces that are described by a set of parameterized variables, including time. The evolution of the

contour is governed by a partial differential equation given by [10]:

$$\frac{\partial}{\partial t}C(u, v; t) = F \cdot \hat{N} , \quad (2.1)$$

where,  $C$  is the contour,  $u$  and  $v$  are parameterized variables,  $t$  is the time variable,  $\hat{N}$  is the unit vector normal to the contour and  $F$  is sum of all force-like vectors acting on the contour. The speed at which the contour evolves is defined by a speed function [10]:

$$g_I(x) = \frac{1}{1 + (NGM_I(x)/v)^\gamma} . \quad (2.2)$$

Here,  $I$  represents the input image,  $NGM_I$  is the normalized gradient magnitude of  $I$ ;  $v$  and  $\gamma$  are user supplied parameters that determine the shape of the monotonic mapping between normalized gradient magnitude and the speed function [10]. The speed function is non negative the contour expands until it reaches the boundary of the ROI, where the speed functions tends to zero. Finally, the force  $F$  on the contour in ITK Snap is given by the function [10]:

$$F = \alpha(P_{obj} - P_{bg}) + \beta\kappa . \quad (2.3)$$

$P_{obj}$  and  $P_{bg}$  are the probabilities that a particular voxel belongs to the ROI or the background;  $\alpha$  and  $\beta$  are the weights that determine the relative contribution of each component,  $\kappa$  is the mean curvature. The user is free to manipulate the parameters to allow to the user to streamline the segmentation process. The user modifiable parameters include the weights  $\alpha, \beta$  and  $\gamma$ , and the mean curvature  $\kappa$ . These variables take up a default value, unless modified by the user, i.e. they do not necessarily require a set of values from the user, but are an additional aid in obtaining a user defined region of interest in the image. The variation caused in the image with respect to the change in values of the aforementioned parameters can be found in Yushkevich et al. 2006 [10].

### 2.3 Material Modelling

The thesis deals with patient specific FEA of femur bone. Hence, the material properties assigned to the femur bone need to be in close agreement to that of the properties in the actual patient's bone. Since *in-vivo*<sup>1</sup> material testing of the bone is not possible, the material properties are derived from the available patient CT-scans. CT-imaging is done using multiple X-rays taken from different angles to get images of different cross-sections. As conventional X-rays are used, the images generated work on the same principle as that of an X-ray image where the beam passing through a denser material gets absorbed more as compared to less dense material [11]. The CT data provides the X-ray attenuation values of the bone tissues which can be further correlated to the bone density [12]. This density is then be used to derive the mechanical material properties using relations from various literature [12–14].

Each pixel in a CT-Scan has an intensity value, also known as the X-ray attenuation coefficient, that varies linearly with the Hounsfield unit ( $HU$ )<sup>2</sup>. The  $HU$  scale is a dimensionless representation of the density of the X-rays absorbed by the material. The  $HU$  are measured at a scale where the attenuation value of the water is assigned to zero while that of the air is assigned -1000, at 25°C temperature and 1 kPa pressure [11]. The calculation of the  $HU$  for rest of the materials is based on the scale:

$$HU = 1000 \times \frac{\mu - \mu_{water}}{\mu_{water} - \mu_{air}} , \quad (2.4)$$

<sup>1</sup>Part of the living.

<sup>2</sup>Named after the founder of CT-scans; sir Godfrey Newbold Hounsfield

where  $\mu$  is the original attenuation value of the material while  $\mu_{water}$  and  $\mu_{air}$  is that of water and air respectively. The  $HU$  is then used to find the  $\rho_{qct}$ . This is done using a calibration phantom which consists of material of known density and  $HU$ . These known values are used to find a linear correlation between each other. This is generally of the form:

$$\rho_{qct} = a + b(HU), \quad (2.5)$$

where,  $a$  and  $b$  are constants. A calibration phantom is a device made of acrylic tubes<sup>3</sup> consisting of known materials that are scanned along with or after the patient's scan. This is used to determine the  $\rho_{qct}$  of the tissue or bone being scanned. The table 2.1 below lists some materials, their density and the proximate  $HU$ . The phantom data was provided by the Radiological department at US Hospital, Linköping.

Table 2.1: Calibration phantom material details

Material Name	Density (g/cm <sup>3</sup> )	Approximate HU value
Water	1	-1000
Polyoxymethylene (POM)	1.41	300
Polyvinylidene Fluoride (PVDF)	1.78	600
Polytetrafluoroethylene (PVDF/Teflon)	2.2	950

B. Helgason, *et.al.* [15] lists a comparison of different Young's modulus-density relations from the literature and the power-law in [13] is shown to have a higher accuracy when used in FE models validated against experimental results. The model showed a linear regression coefficient of 0.962 when comparing the FEA results with experimental data from 496 samples. This is a pooled sample data containing trabecular and cortical bone and is therefore selected for this study. The power-law reads:

$$E = 10.5\rho_{ash}^{2.57}, \quad (2.6)$$

where  $E$  = Young's modulus in GPa and  $\rho_{ash}$  = ash density of the bone in g/cm<sup>3</sup>.

A study conducted by E. Schileo *et.al.* [14], consisting of sixty specimens taken from three human and three bovine femurs, gives an accurate conversion of  $\rho_{qct}$  to  $\rho_{ash}$ . The conversion is:

$$\rho_{ash} = 0.07894 + 0.8772(\rho_{qct}). \quad (2.7)$$

This equation has been manipulated to match the input method for the material modelling file. Using these above equations the material property of the bone is assigned to individual element of the FE model. This makes the material assigned to the complete model heterogeneous and isotropic.

<sup>3</sup>For this particular study, the phantom material may change depending on provider.

# 3

## Method

### 3.1 Image segmentation

The femur model was extracted from anonymous patient CT data provided by the orthopaedic department of US Hospital, Linköping. The segmentation process was done using the software ITK-Snap. The theory of the segmentation process is explained in the section 2.2. First, the CT-images were imported into ITK-Snap as DICOM images. The first operation performed was to adjust the contrast and threshold parameters of the image to obtain a clear definition between the bone components and rest of the image constituents. The original DICOM image and the contrast adjusted DICOM image are depicted in the figure 3.1a and figure 3.1b Once the contrast was deemed satisfactory, the active contour segmentation

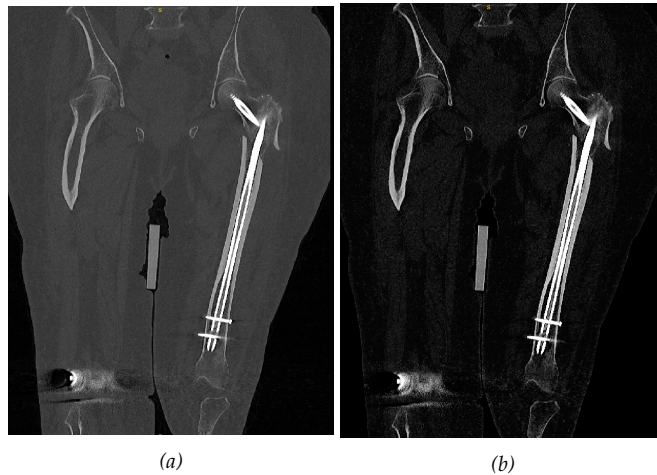


Figure 3.1: (a) Original DICOM image; (b) Contrast adjusted DICOM image

process(Snake) was initiated. The software prompts the selection of the ROI, which eliminates unwanted areas of the 3-D image. This selection is depicted in figure 3.2 by the region bounded by the red box. The 3-D model required was of the left femur (one without implant), which was selected.

Next, the bone material was manually labelled (or classified) to familiarize the algorithm with the voxel intensity that is to be segmented. Figures 3.3a and 3.3b depict two different slices of the image. The bone material is assigned the 'red' label, while the background is assigned the 'blue' label. This helps the classifier understand the difference in required labels and the unwanted labels for the final 3-D model. The user can assign multiple labels in the image based on the requirement. Each label can be then segmented separately or as a part of the same model with separate surfaces. Finally, the contours were manually placed on different slices throughout the image. These contours appear in the form of spherical

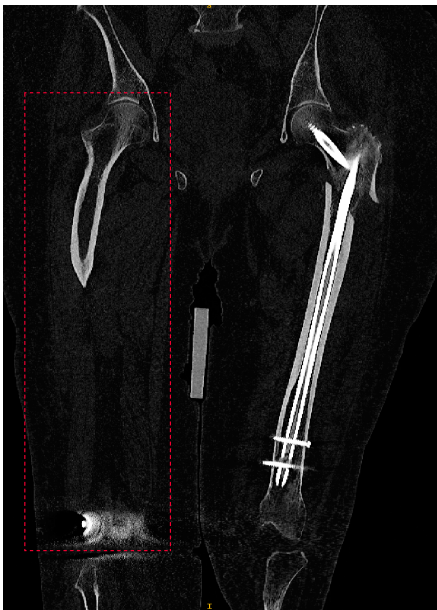


Figure 3.2: Selection of ROI; the red box depicts the selection

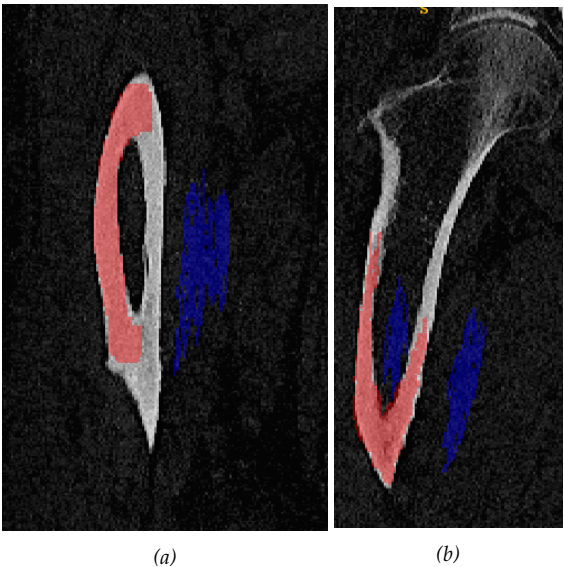


Figure 3.3: (a) and (b) depict label classification in two different slices of the image

bubbles, as seen in figures 3.4a and 3.4b. Once the user places a sufficient number of these bubbles across the image slices, the segmentation process is executed. As explained earlier in section 2.2, the contours start evolving once the algorithm is initiated. This evolution is based on forces acting on the contour. Essentially, an outward force acts on each contour, which forces it to initially expand. These outward forces remain dominant until the contour reaches a boundary with a different label or intensity. At the boundary, inward forces act on the contour, forcing it to stop expanding. For example, in figure 3.4a and 3.4b, the 'red' region encompassed under the bubble (contour) is the label assigned to the bone material (figure 3.3a and 3.3b), which is what needs to be extracted. The contour starts expanding, until it reaches the boundary of the bone, which has been assigned the 'blue' label. Since this zone has a different label and intensity, the contour stops expanding at the boundary of the bone. The eventual desired scenario is to have all the bone regions across all slices of

the scan to under the 'red' label, which is why these contours are placed in multiple places across all slices. It is important to note that since a lot of factors such as complexity of the geometry, boundary definitions and image quality come into play, the model generated by the automatic segmentation algorithm usually needs manual segmentation by the user to be exact and complete. Hence, the final model obtained was a mixture of automatic and semi-automatic methods. The final model generated from ITK Snap is shown in figure 3.5, which is a surface mesh file.



Figure 3.4: (a) and (b) depict active contours placed in two different slices of the image

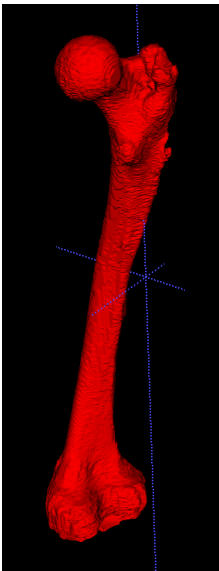


Figure 3.5: Final model obtained from ITK Snap

3.2 CAD design of Implants

The design of the implants is based on the the T2 Recon nailing system R1.5 from Stryker Corporations , for hip and femur fractures. The first type is known as the *recon screw set*, the second type is called *antegrade screw set*. The screws used in both the nailing systems are the same. The 5 mm fully threaded locking screws (figure 3.6a) are used in the distal(bottom) region of each nail/rod. The nail/rod of both the systems is similar in design in terms of curvature (1.5 m antecurvature radius), length (380 mm), the placement and size of the holes in the distal region, along with the radius of the top and bottom section of the nail itself (figure 3.6c). The key difference between the two systems is the placement, size and orientation of the holes in the proximal(top) region of the nails. The placement of screws in the Recon model is such that two 6.5 mm cannulated lag screws (figure 3.6b) are inserted around 30 mm from the top of the nail, which are oriented in a manner that these screws penetrate the femur neck (as centric as possible). The screws must be long enough to cover a significant diametric length of the femoral head. In the Antegrade model, the positioning of the proximal hole to the top of the nail is relatively lower when compared to the Recon model. The hole is also oriented differently in an angular sense and locking screws are used in the Antegrade model in the proximal as well as distal holes. The placement of the proximal screw is such that it protrudes out from the trochanter minor/lesser trochanter.

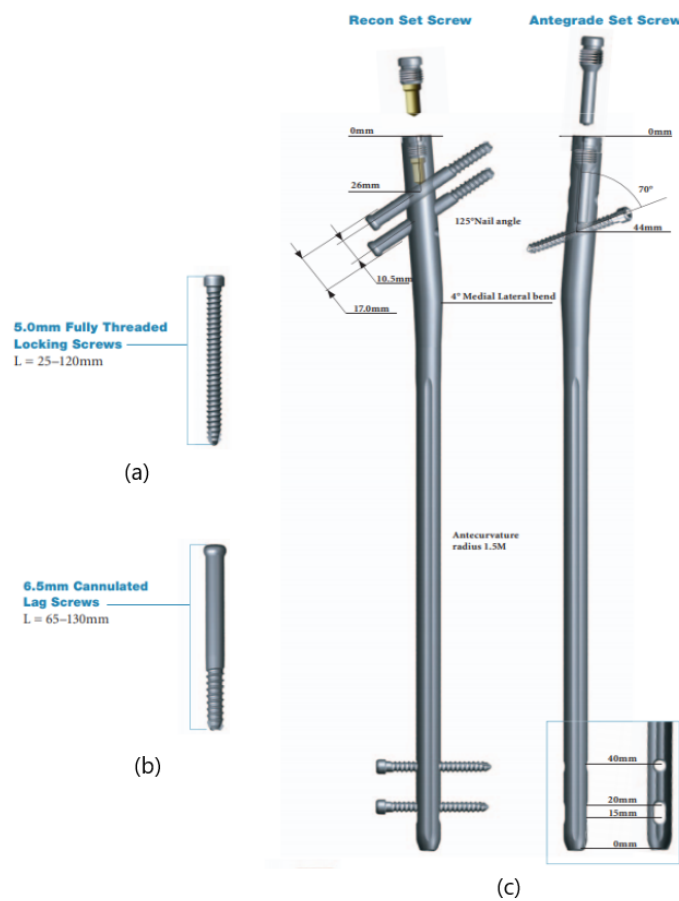


Figure 3.6: (a) 5.0 mm fully threaded locking screw (b) 6.5mm cannulated lag screw (C) Description of the Recon and Antegrade nails

The design and assembly of both sets of nails and screws was carried out in Solidworks (version 2019, Solidworks Corp., Waltham, Massachusetts, USA). The only difference be-

tween the CAD models and the recommended design was that the heads of the screws were removed without compensating the length of the screw. This was done since meshing the assembly caused some complications in terms of element size selection at the head of the screws (distorted elements). The only solution was to reduce the element size, which increased the overall quantity of elements beyond the allowable number of elements in the student versions of the FE softwares used. Hence, a choice was made to remove the screw heads in order to simplify the meshing process. The assemblies of the Recon system and the Antegrade system are presented in figure 3.7a and 3.7c respectively. Figures 3.7b and 3.7d represent the 1.5 m antecurvature radius that is depicted in the description of these nails (figure 3.6). This curvature is applied to accommodate the similar curvature that is visible in the femur bone in the above figures.

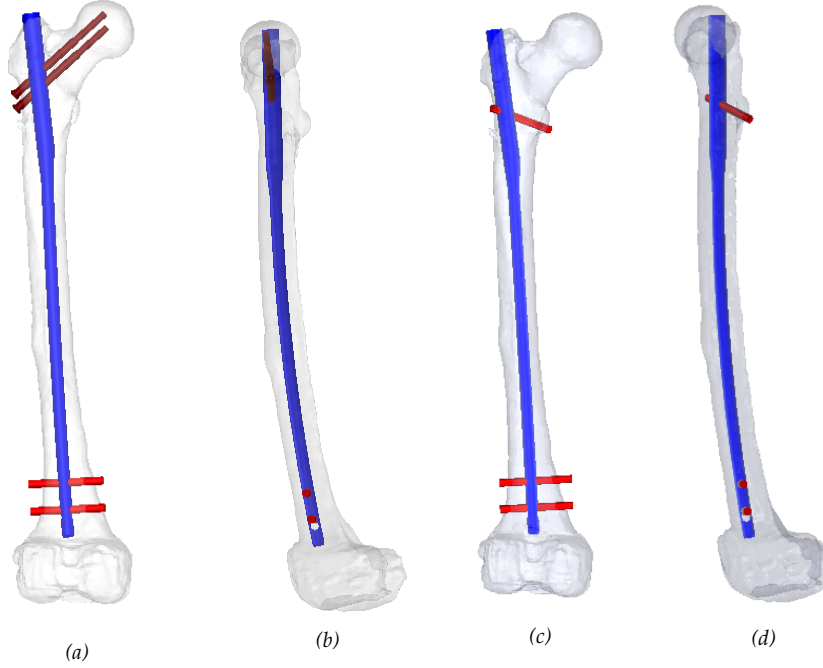


Figure 3.7: (a)Recon fixation assembly - front view and (b)Recon fixation assembly - side view, with locking screws(bottom), cannulated screws(top) and the bone; (c) Antegrade fixation assembly - front view and (d) Antegrade fixation assembly - side view, with locking screws (top and bottom) and the bone

### 3.3 Meshing

ITK-snap exports the final model as a surface mesh file of *.stl* format. This consists of a number of errors and faults in terms of future meshing and solid conversion processes. Initially, exporting the surface mesh into Meshlab (version 2020.12) helped rectify these issues. MeshLab is an open source software used to create, modify and render 3D meshes [16]. The initial mesh file was cleaned off duplicate vertices, null faces and manifold edges. This made certain that the meshing at a later stage would be simpler and the surface generated is watertight which makes it possible to convert the mesh into a solid. Even after this process, the resultant mesh was still very fine with 609,232 faces and 304620 vertices, which resulted in very high computational time in just exporting the file from one software (which is a reasonably significant part of the process from the initial CT image to obtaining the final FE model). Also, such high resolution in the meshed model is not a desired trait as the time taken for converged solution time would be very high, not to mention computational power required. To overcome this, the mesh was made coarser and the surface was smoothened. The figure

3.8 below show the transformation of the initial mesh to the final mesh that is further taken forward.

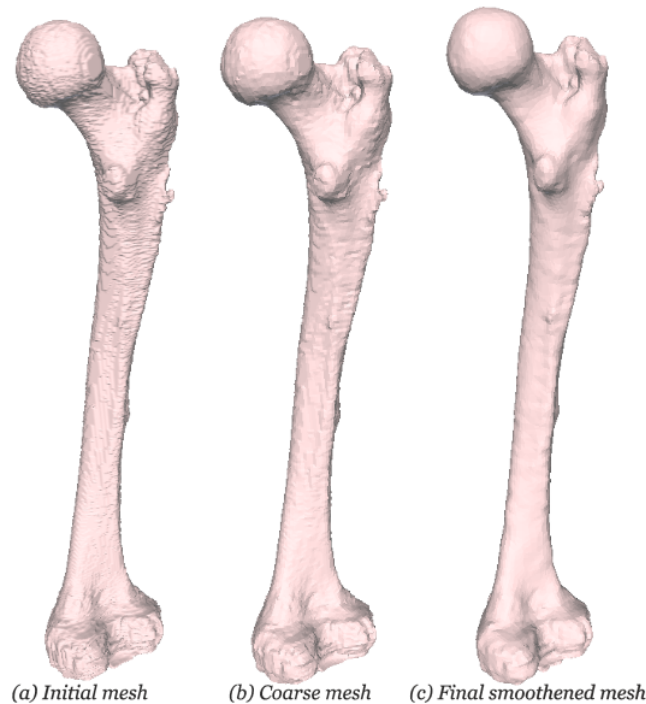


Figure 3.8: The figure shows the initial to final mesh transformation; (a) Initial mesh with 609,232 faces and 304,620 vertices; (b) After making the mesh coarse, 45,876 faces and 22,938 vertices; (c) Making the mesh more coarse and smoothing it, 15074 faces and 7539 vertices

The surface mesh was then imported into Solidworks. Here the mesh was converted to surfaces. This was done to assemble the bone with the implant and to ensure proper position. The Solidworks assembly module was used in this step. Once this was finalized, the assembly was then exported as .stp file into Hypermesh (version 2017.3, Altair Engineering, Inc., Troy, USA).

The final software used for fixing the errors in the mesh was Hypermesh, as it provided the maximum freedom in generating and modifying the mesh. Also, the factor of previous experience in using the software made it an obvious choice. First, the assembly was imported into Hypermesh, then the intermedullary nail and screws were organized into one component to simplify the meshing process. To integrate the bone and the implant as one solid model, the boolean operation was used to remove the bone material intersecting with the implant. This produced clean cut and shared surfaces (figure 3.9). This helped ensure that the mesh generated was continuous. Next, the *autocleanup* process is used with target element size of 6mm is run for both the models to reduce the elements with errors.

The components are meshed in the Abaqus user profile, as the analysis is eventually performed in Abaqus (version 6.14-2). The elements used are second order R-tria elements or C3D10M elements. The elements vary in size from 6 mm to 1.8 mm depending on the curvature of the surface and the sizes of other elements in its proximity.

Once the meshing was completed, the parts (bone and implant) were exported individually as .inp file. The figure 3.10 below shoes the final meshed model for the two implant types and the bone.

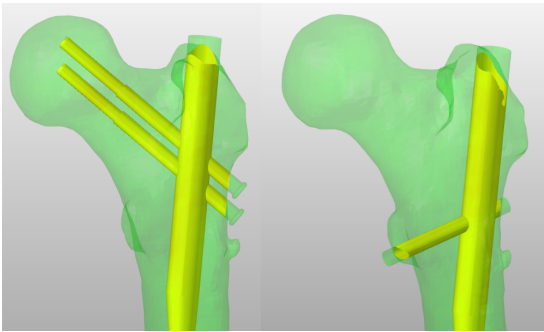


Figure 3.9: The yellow surfaces represent shared surfaces between two parts

Table 3.1: Mesh details

Model Type	Number of Elements
Bone + Recon Implant	112719
Bone + Antegrade Implant	95291
Bone	54619

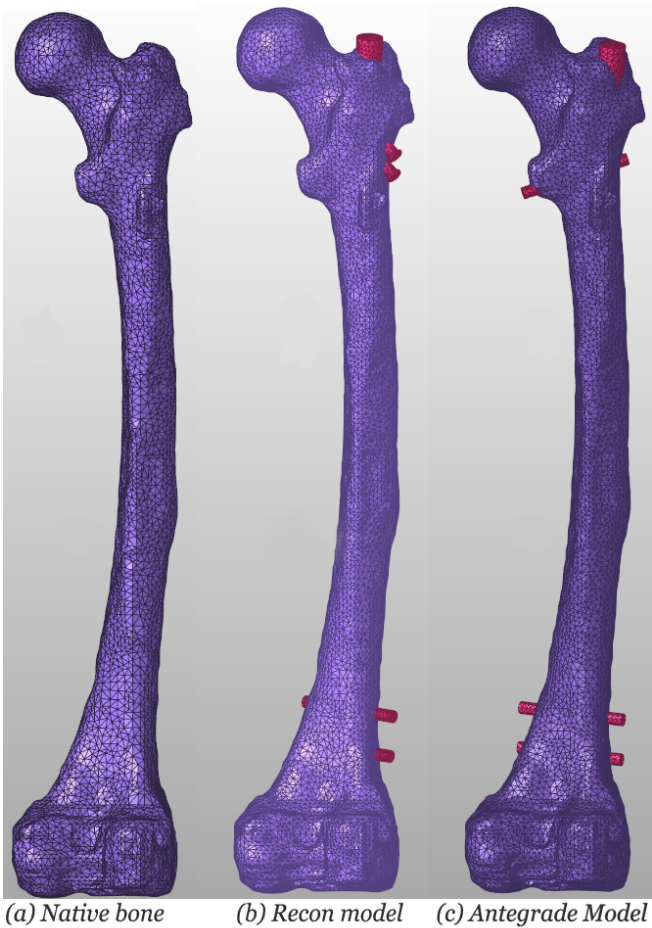


Figure 3.10: (a) Bone without implants; (b)Bone with Recon locking; (c)Bone with Antegrade locking

### 3.4 Material Mapping

For the purpose of assigning materials to the meshed components, Bonemat (version 3.2) was used. Bonemat is a software developed to map the material property of the bone, derived from CT images, onto the FE mesh. Here the original DICOM image was imported and cropped to the required ROI. FE mesh file of the bone was then imported into it and aligned to superimpose onto the DICOM images. Similarly, the implant mesh was also imported and aligned. The figure 3.12 shows the aligned bone and implant mesh.

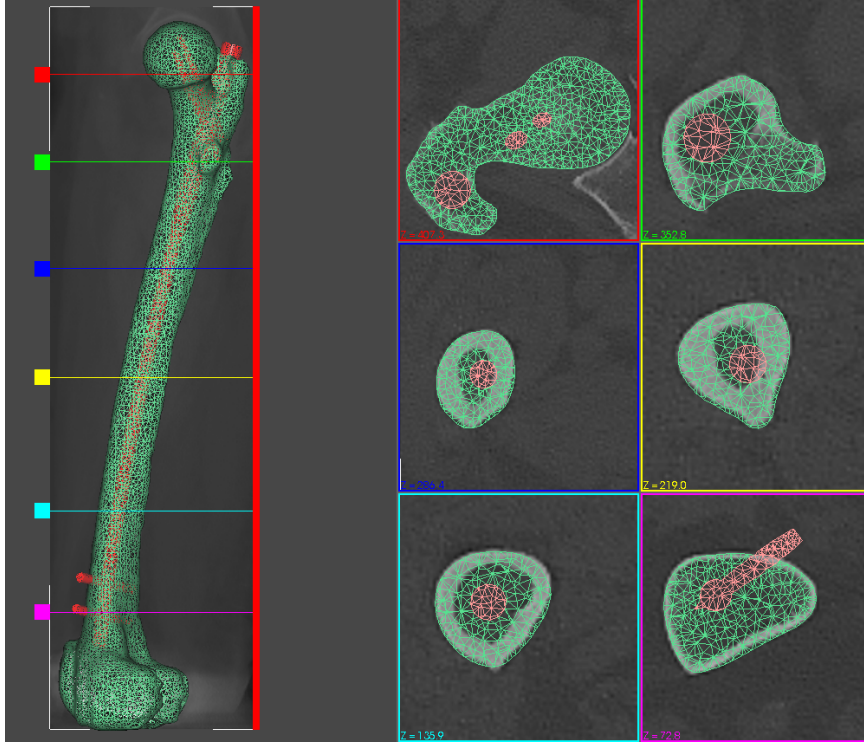


Figure 3.11: Each section view correlated to the colored line; Green mesh : Bone ; Red mesh : Implant

To assign the material property, Bonemat's configuration file needs to be loaded onto the software. This file consists the equations for converting the  $HU$  to  $\rho_{qct}$  and then a correction equation where  $\rho_{qct}$  is converted to  $\rho_{ash}$  using equation (2.7). This is then used to derive the Young's modulus for each element by equation (2.6). The derivation of the relation between the  $HU$  and  $\rho_{qct}$  was done by converting the image slice with the calibration phantom into a matrix of the size of image resolution where each value correlates to the pixel's intensity at that location. This matrix was then converted into  $HU$  using a linear conversion (see Appendix I for more details). This gives us the coefficients for equation (3.1) as:

$$a = 1.0002, \quad b = 1.3477 \times 10^{-3}.$$

Substituting them in equation (3.1) we get:

$$\rho_{qct} = 1.0002 + \left(1.3477 \times 10^{-3} \times HU\right). \quad (3.1)$$

This equation can be validated by substituting the  $HU$  for water ( $HU=0$ ) giving  $\rho_{qct}$  as  $1.0002 \text{ g/cm}^3$  which is the density of water.

Here, there are two options on assigning the material property - either the  $HU$  is integrated over the element volume for pixels that fall under that element and then the Young's modulus is calculated and assigned, or the Young's modulus of each pixels is first calculated

Calculating radiological density from HU value (Eq 3.1)

Calculating ash density from radiological density (Eq 2.8)

Calculating Young's modulus from ash density (Eq 2.7)

Integrating Young's modulus over the element volume.

CT densitometric calibration

$\text{RhoQCT} = a + b * \text{HU}$

a

1.00024

b

0.001377

Correction of the calibration

$\text{RhoAsh} = a + b * \text{RhoQCT}$

☒ Apply calibration correction

Single interval

Single interval

a

0.07894

b

0.8772

Three intervals

Density-elasticity relationship

$E = a + b * \text{RhoAsh}^c$

Minimum Elasticity Modulus

1e-06

Single interval

Single interval

a

0

b

10500

c

2.57

Three intervals

Young's modulus ( E )

E integration

Integration steps

4

Gap value

50

Figure 3.12: Bonemat configuration file, showing inputs for the constants

and then integrated over the element volume. Taddei *et.al.* [12] showed that numerical integration of Young’s modulus over the element volume produced better results when the principle strain is compared between the FEM results and the experimental ones. Therefore this process has been followed here as well. The bone is assigned the Poisson’s ratio of 0.3 [12]. Once the configuration file has been setup the material properties are assigned. This creates a new mesh file in Bonemat with the assigned material properties. This mesh file is then exported as *.inp* file. Similarly the aligned implant file is also exported.

3.5 FE Model Setup

The FE model setup and solving was carried out in Abaqus (version 6.14-2). The bone and the implant mesh files were imported into Abaqus from Bonemat, as separate models. The implant is assigned a Young’s modulus of 110 GPa (Ti<sub>6</sub>Al<sub>4</sub>V). The implant model’s objects were then copied into the bone model, transferring both the parts into the same model. Since both the parts were previously aligned in Bonemat, they fell in the correct relative orientations in the assembly.

Bone and the implant were constrained together using ‘tie’ constraint between the shared surfaces. These shared surfaces, inner surface for the bone and the external surface for the implants, were selected initially (figure 3.13) and saved as sets of elements, for ease of selection. In the relationship between the two surfaces, the implant surface was assigned the master surface and the bone surface as the slave.

The nodes on the distal ends of the femur bone have been fixed in *x*, *y*, and *z* directions. The loads were initially applied as concentrated forces at a single node near the region of contact, this caused several issues which are discussed later. To avoid these issues, a refer-

16

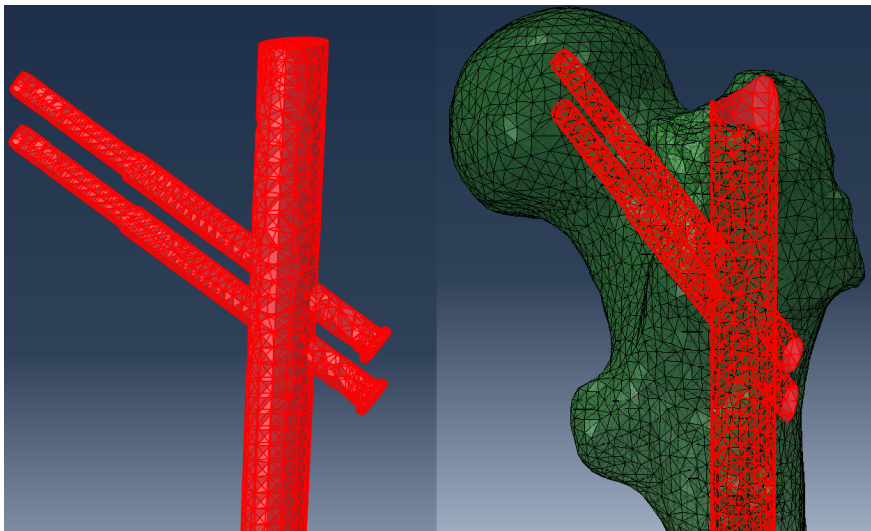


Figure 3.13: Selected surfaces for constraint

ence point (RP) was created above the region of contact and the surrounding nodes were connected to it using multi-point constraint (MPC) beam connections, see figure 3.14. This helped distribute the load and avoid stress concentration on a single element. This type of connection helps constraining the displacement and the rotations of the master node, the RP in this case, with the slave node-set, the selected nodes on the femoral head [17].

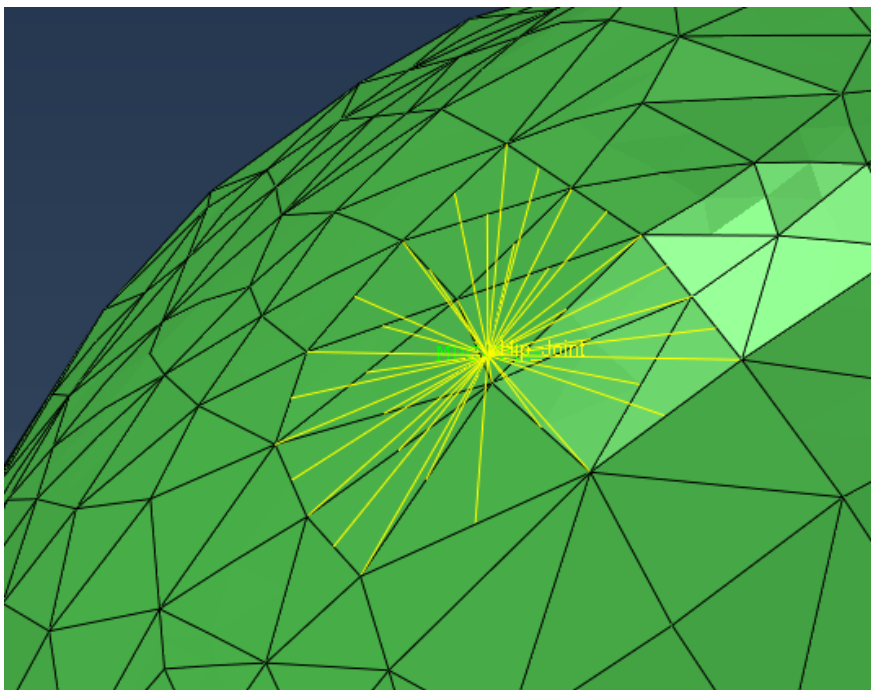


Figure 3.14: MPC tie constraint between RP and node-set for hip joint load

**Loading states with peak loads during everyday activities**

The loads chosen to analyze the model of the femur bone have been obtained from Bergmann *et. al.* [18], that studies the forces acting on hip implants. The study was performed among a

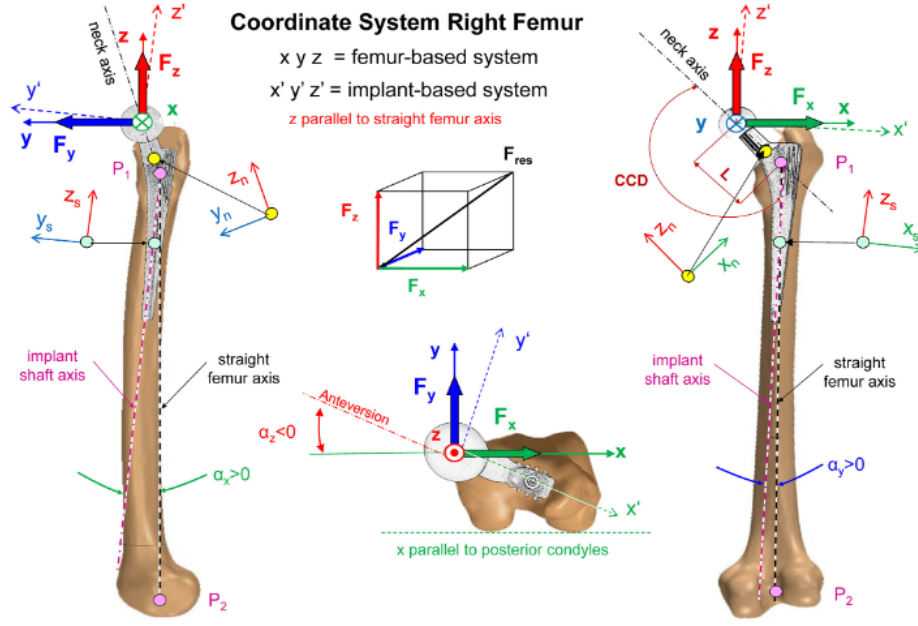


Figure 3.15:  $x, y, z$  = axes of femur coordinate system.  $x$  = parallel to posterior contour of condyles.  $P1$  = intersection of neck axis and femoral midline.  $P2$  = middle of intercondylar notch.  $z$  = straight femur axis between  $P1$  and  $P2$ . Force components  $F_x, F_y$  and  $F_z$  act in directions  $x, y$  and  $z$ . Moment components  $M_x, M_y$  and  $M_z$  turn clockwise around  $x, y$  and  $z$ . The implant is turned clockwise by angles  $\alpha_z, \alpha_y$  and  $\alpha_x$  around the femur axes  $z, y$  and  $x$ .  $\alpha_z$  = anteversion of neck (negative).  $x', y', z'$  = axes of implant.  $x_n, y_n, z_n$  = coordinate system at distal end of implant neck.  $x_s, y_s, z_s$  = coordinate system of stem 80 mm below head centre [18]

group of 10 patients, all of which had undergone hip implant procedures. Figure 3.15 depicts the coordinate system  $[x y z]$  used to describe these loads, with the origin taken as the centre of the femoral head. The coordinate system  $[x' y' z']$  represents the coordinate system of the hip implant. The loads are measured on the implant, and converted to equivalent loads acting on the femur head. The conversion of these implant loads to femur loads is defined by the following equations [18]:

$$F_i = \mathbf{T} \mathbf{F} , \quad (3.2)$$

$$M_i = \mathbf{T} \mathbf{M} , \quad (3.3)$$

where  $F_i$  is the force matrix and  $M_i$  is the moment matrix acting on the implants ( $[x' y' z']$  coordinate system),  $\mathbf{F}$  and  $\mathbf{M}$  are converted equivalent loads on the femoral head ( $[x y z]$  coordinate system) and  $\mathbf{T}$  is the calculated transformation matrix given as [18]:

$$\mathbf{T} = \begin{bmatrix} 0.9671 & -0.2159 & 0.0251 \\ 0.2133 & 0.9738 & 0.0783 \\ -0.0414 & -0.071 & 0.9966 \end{bmatrix} \quad (3.4)$$

Bergmann *et. al.* [18] provides the average and peak values of these loads in various everyday activities such as sitting down, standing up, knee bend, walking, climbing stairs, descending stairs, cycling and jogging. Since the patient being examined in this master thesis study is an elderly woman with a fracture in the shaft of the femur in addition to being osteoporotic, moderately strenuous activities such as walking are used for the relative comparison between the two implant types. The load cycle applied in this study is a 12 second

walk, in which the subject completes 3-4 gait cycles. The data for this loading is taken from the orthoload database (<http://www.orthoload.com/database>), which contains data recorded in testing hip implants. A graphical representation of the hip contact force components is visible in figure 3.16.

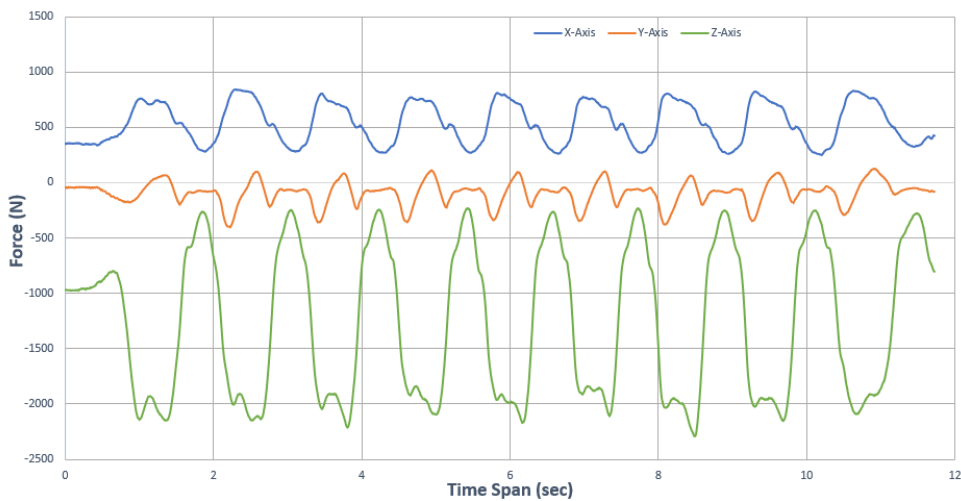


Figure 3.16: Force components of the applied hip load, in  $[x\ y\ z]$  coordinate system of femur model

Loading with muscle loads

The second loading condition used for verifying the material property of the bone model is taken from Taylor *et. al.* [19] and is also used in Gustafsson *et. al.* [20]. The loading state is comprised of hip contact loads taken from the stance phase of the gait cycle, along with forces due to three major muscle groups - abductor, ilio-tibial tract and iliopsoas. The positioning of the loads can be seen in figure 3.17 and values of the loads are logged in the table 3.2.

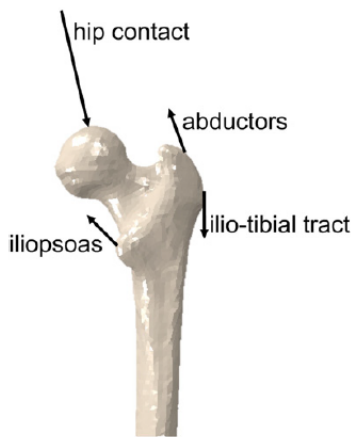


Figure 3.17: Placement of hip contact along with the muscle groups [20]

Boundary conditions

The essential boundary condition is a complete fixation of a node set on the surface on the femoral condyles. This is the lowest point of the femur; the surface that is in contact with the

Table 3.2: Load values of hip contact and three major muscle groups during the stance phase of the load cycle

Load type	Load Components [N]			
	$F_x$	$F_y$	$F_z$	$F_{resultant}$
Hip contact	-616	-171	2800	2872
Abductors	430	0	-1160	1237
Ilio-tibial tract	0	0	1200	1200
Iliopsoas	78	560	525	771

tibia at the knee joint. It is constrained in all translations and rotations to prevent rigid body motion. The positioning of this constraint is depicted in figure 3.18.



Figure 3.18: Fixed support BC at the femoral condyle surface in the distal region of the femur

# 4 Results

## 4.1 Bonemat

The exported mesh model from bonemat contains a number of material sets that have been assigned to the bone mesh. Since the mesh is slightly different for the three bone models (Recon, Antegrade and Native model), the number of material sets vary slightly. This has been listed in the table 4.1 below along with the range of Young's modulus in each of them. Figure 4.1 shows the mapped Young's modulus on the no-implant bone mesh.

Table 4.1: List of different material sets.

Model Type	Number of Material Sets	Range of Young's Modulus (GPa)
Recon Model	1030	0.27-54.99
Antegrade Model	1010	0.13-54.99
No-Implant Model	988	0.11-54.99

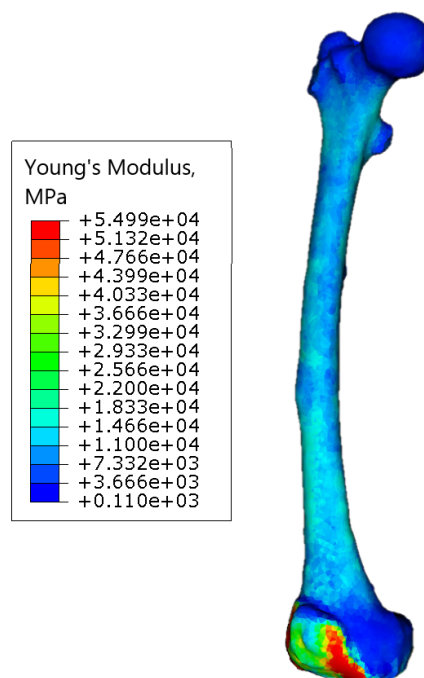
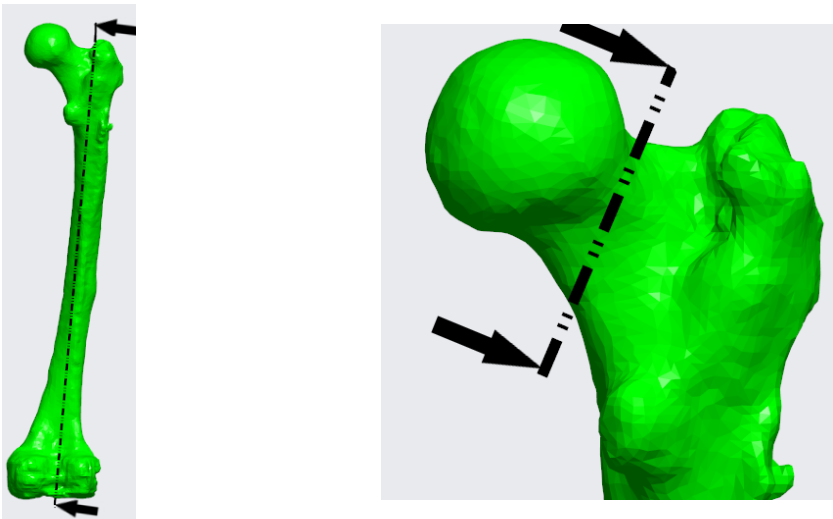


Figure 4.1: Mapped Young's modulus on the no-implant bone model

4.2 Finite Element Analysis.

After running the simulations for the two load cases, the following chapter gives the results for the three models. Firstly, the Native bone model along with the Recon and Antegrade models have been simulated using the load case from Taylor *et. al.* [19]. This was done to compare and verify the bone material model with the strain data taken from Gustafsson *et. al.* [20] where a similar model set-up is used. Secondly, the load case from Bergmann *et.al.* [18] is used to simulate the Recon and Antegrade models with are compared with each other. Here the material property assigned to the bone makes it heterogeneous isotropic component. The results below are in the form of maximum principal stress and strain contours. These quantities are used to compare the models as the material formulation used have been validated against the same. The legends accompanying the contours have been manipulated to provide consistency through out the comparing models. Also, this helps remove values generated due to localized stress concentration which occur in the region where the load is applied. This stress concentration does not happen in reality as the load is much more evenly distributed.

The following subsections contain section views of the model for better understanding and analysis of the results. Figure 4.2 shows the position and the orientation of the section view planes.



(a) Lateral section view plane

(b) Femoral neck section view plane

Figure 4.2: Position and orientation of the section view planes

Loading with muscle forces

Figure 4.3 below show the maximum principal strain through the femoral neck region for the three model. It is clearly seen that the Antegrade model (figure 4.3c) shows a higher strain through the neck as compared to the Recon and the Native bone model. Based on the contour distribution, Antegrade model shows higher strains in the proximal neck region which spreads evenly through the trochanteric fossa. For the Native bone (figure 4.3a), the strain through the posterior neck reduces much quicker compared to Antegrade model. Recon model (figure 4.3b) shows much more localized strain on the proximal neck which reduces to minimum as we move towards the proximal neck region. A point of interest here is that for Antegrade and Native bone model the region on either side of the lesser trochanter show much higher strain as compared to the Recon model.

For the Native bone model the maximum principal strain through the neck is in the range of  $10E-3$  to  $6E-3$  while that of the Recon and Antegrade are in the range of  $7E-3$  to  $4E-3$  and  $14E-3$  to  $7E-3$  respectively.

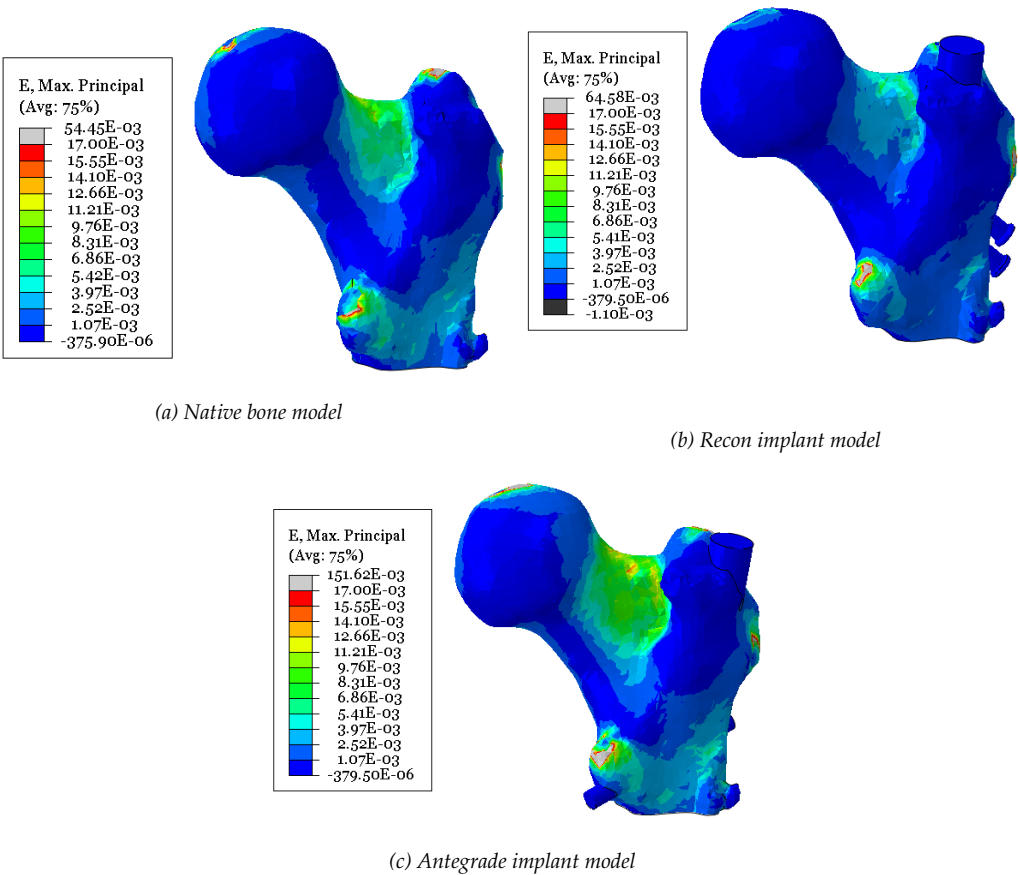


Figure 4.3: Maximum principal strains in the neck region

Figure 4.4 plots the contour of the maximum principal stress in the femoral neck. Antegrade model, in figure 4.4c, experiences a higher principal stress on the proximal region of the neck which extends towards the posterior neck region. For Recon and Native bone model, seen in figure 4.4b and 4.4a, show similar stress distribution, with Recon model containing more dispersed and reduced stress when moving from proximal neck region to posterior neck region. As noted earlier in figure 4.3, the principal stress is seen accumulating on the lateral region of the greater trochanter and extending down to lesser trochanter for the Native bone model and the Antegrade model.

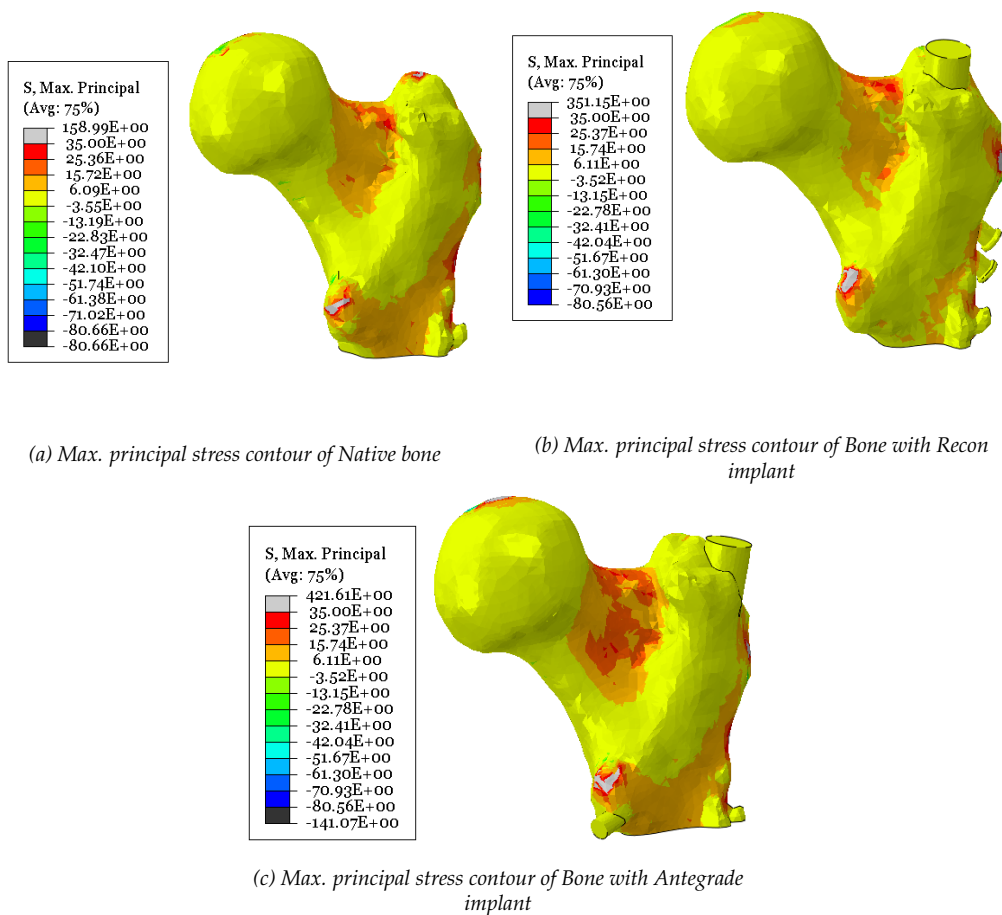


Figure 4.4: Maximum principal stress in the neck region

Figures 4.5-4.10 show the stress strain contour over the complete model. These figures show the anterior, posterior and the lateral section view of the models.

All three models experiences major strain and stress in the distal diaphysis region of the bone. These stresses and strains are continuous throughout the length of the bone, decreasing towards the proximal end of the diaphysis. The greater trochanter in Antegrade model and the Native bone model, seen in figure 4.7(c) and 4.5(c), show a substantially higher strain value as compared to the Recon model (figure 4.6(c)). The intermedullary nail in the Antegrade model also shows an increase in strain in the same region, while this is not the case for the intermedullary nail in the Recon implant. The value of strain for the Recon model in the greater trochanter region, is in the range of  $2E - 3$  and lower, while it is between  $5E - 3$  and  $2E - 3$  for Antegrade model and the Native bone model.

Considering the femur head for all the three models, the Antegrade model shows a much higher distribution of strain through it which increases when moving towards the neck and the trochanteric fossa. In Recon implant when viewed from the posterior side (figure 4.6(b)) the femur head shows minimal strain as opposed to the Antegrade model.

Through out the models the stress is much more evenly distributed then strain. There are a few stress concentration spots which can be seen in all three models at the same location. They appear at the distal end of the diaphysis in the posterior region. The stresses through the implants are consistent through out both the Recon and the Antegrade model. But it can be seen that the intermedullary nail in the Recon model experiences an increase in stress in the distal posterior region, while that in the Antegrade model does not.

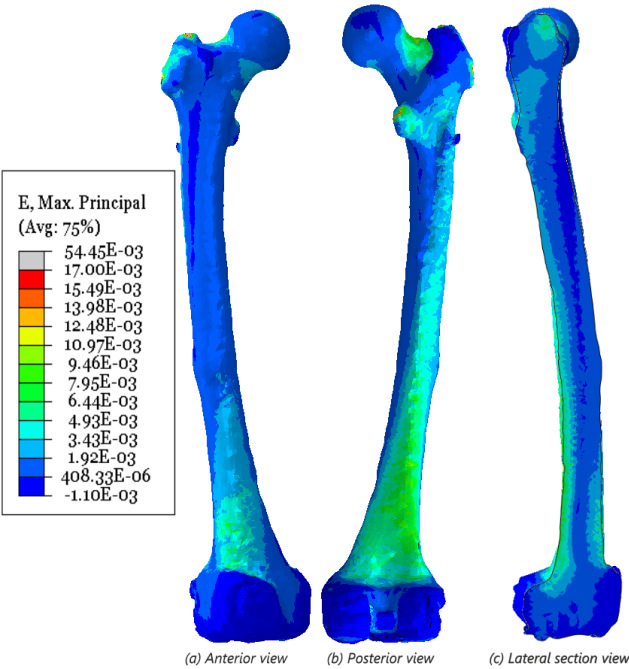


Figure 4.5: Max. principal strain across the shaft for Native bone

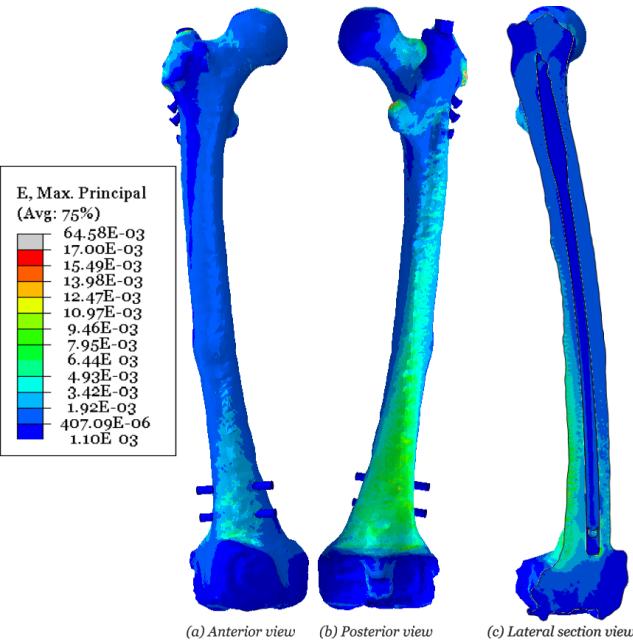


Figure 4.6: Max. principal strain across the shaft for bone with Recon implant

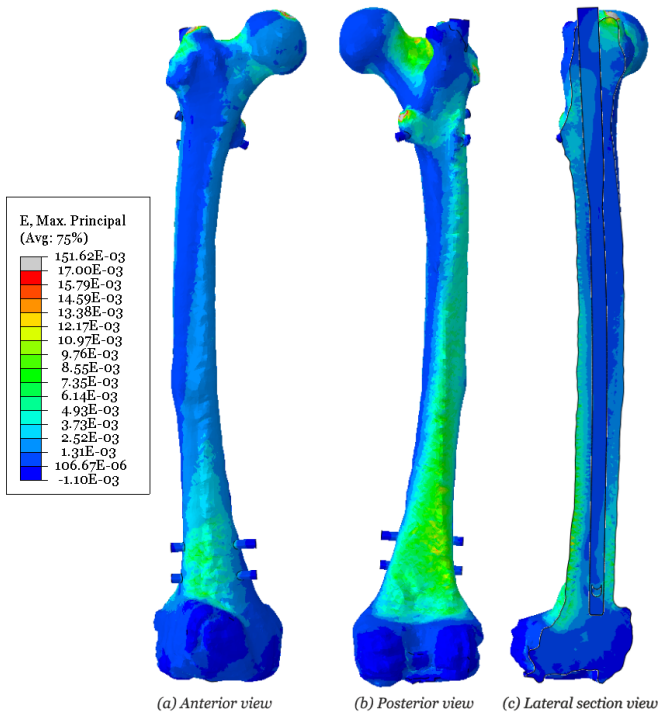


Figure 4.7: Max. principal strain across the shaft for bone with Antegrade implant

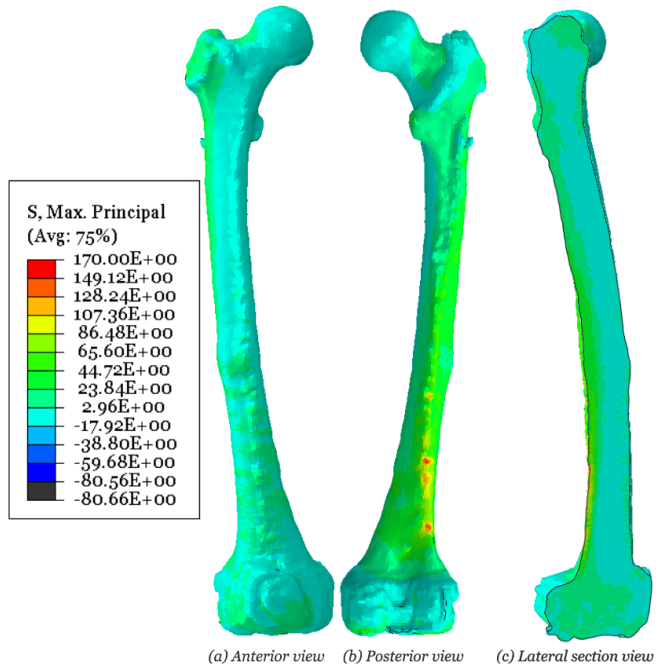


Figure 4.8: Max. principal stress across the shaft for Native bone

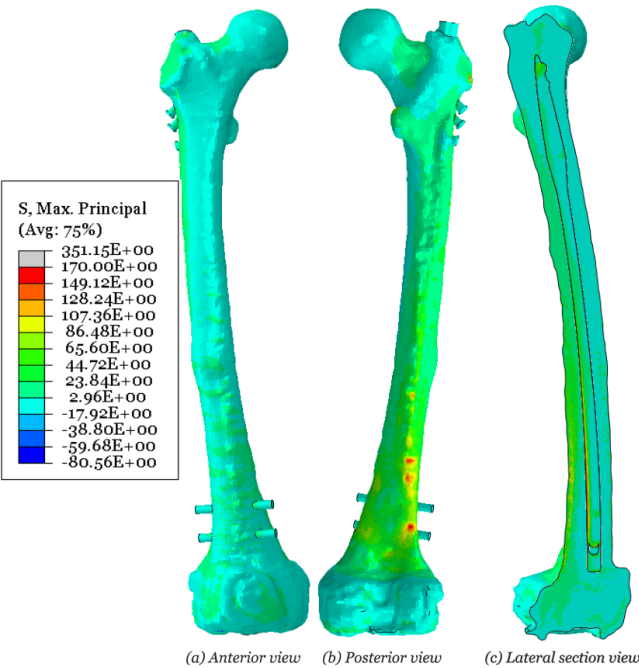


Figure 4.9: Max. principal stress across the shaft for bone with Recon implant

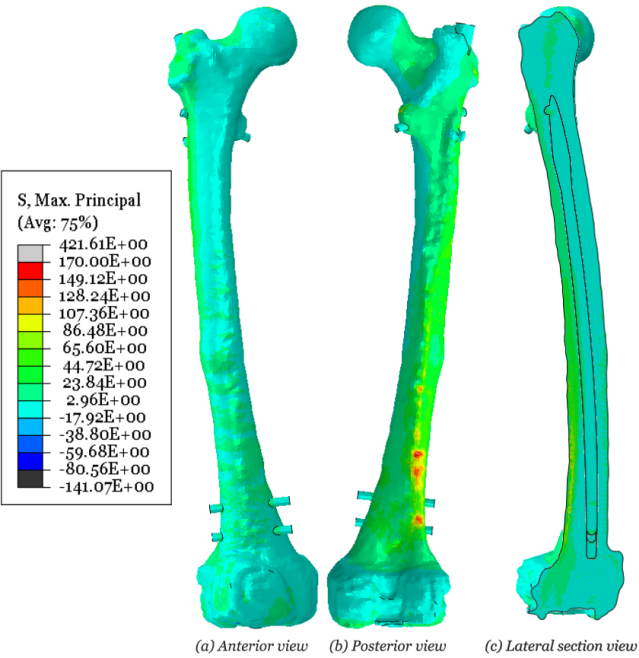


Figure 4.10: Max. principal stress across the shaft for bone with Antegrade implant

Loading without muscle forces

This section shows the results obtained when the Recon and the Antegrade model are simulated under normal walking forces. These forces have been applied at the femur head as described in section 3.5

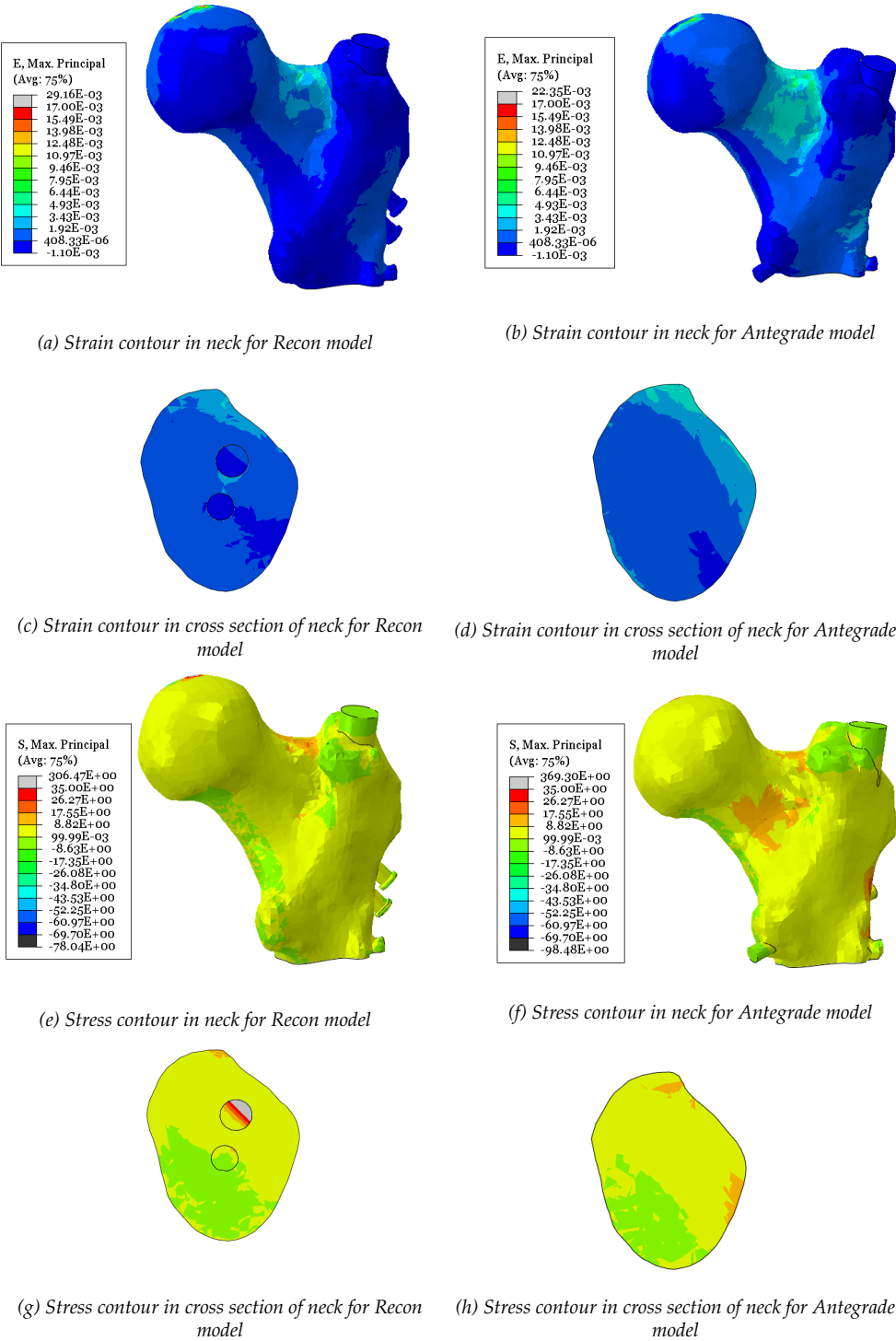


Figure 4.11: Stress and strain across femur neck for loading without muscle forces

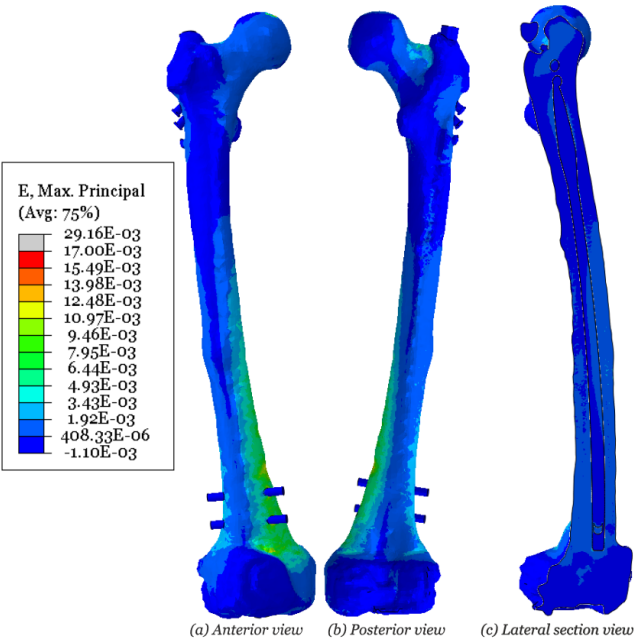


Figure 4.12: Max. principal strain across the shaft for bone with Recon implant

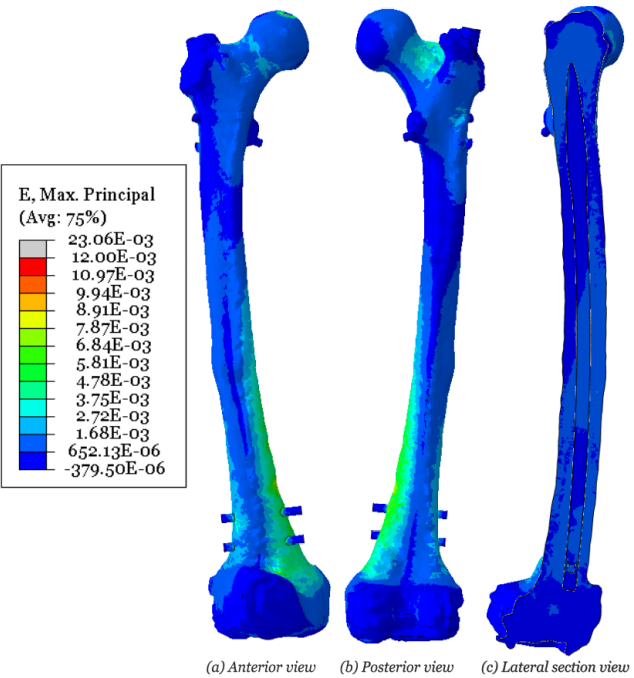


Figure 4.13: Max. principal strain across the shaft for bone with Antegrade implant

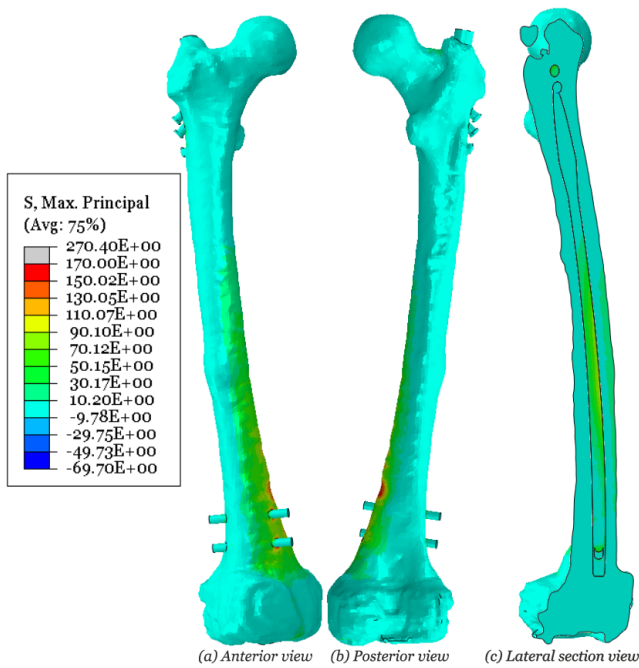


Figure 4.14: Max. principal stress across the shaft for bone with Recon implant

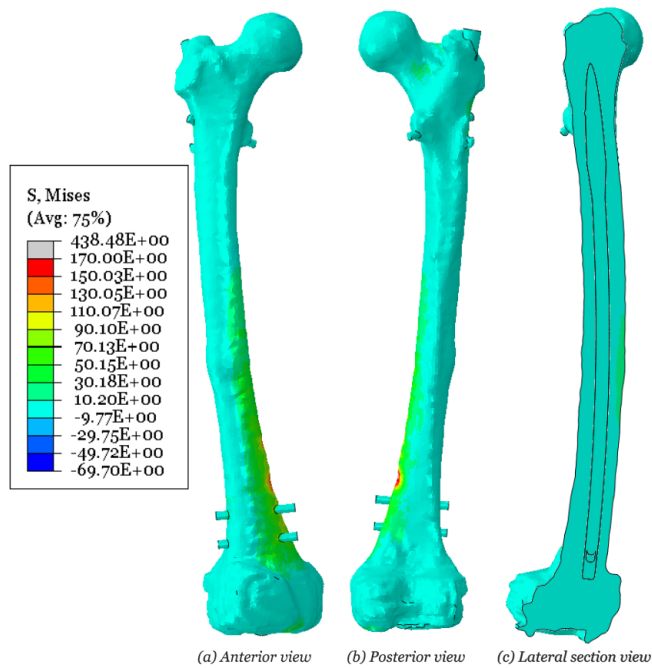


Figure 4.15: Max. principal stress across the shaft for bone with Antegrade implant

These forces do not include muscle forces and are only applied on the femur head. Figure 4.11 shows the stress and strain during a normal walking cycle without the muscle forces. It can be seen in figure 4.11a and 4.11b that the Recon model shows much lower strain in the neck region then the Antegrade model. The section view of the neck region with the strain contours, seen in figure 4.11c and 4.11d, also corroborate with the results from the previous loading conditions and provide an insight into the cross-sectional distribution of the strain through the neck. It is interesting to note that the strain in the bone, between the two recon

nails is increased. For the Antegrade model, since there is no nail through the femoral neck the strain is much more distributed. Similarly the stress through the neck, seen in figure 4.11g and 4.11h, is much more evenly distributed for the Antegrade model. In Recon model the stresses in the distal neck region are much lower than in Antegrade model as the majority of the stress is experienced by the recon nails that pass through the neck, especially the top nail.

Figures 4.12-4.15 show the overall stress and strain contour of the models. Similar observations, as done under previous loading condition, can be made here. The greater trochanter region shows a higher strain for the Antegrade model. Also, the majority of the strain and stress occurs in the distal diaphysis region of the bone. Though, one point to note here is that the implants, seen in the lateral section view in figures 4.12(c) and 4.13(c), show a higher strain in the medial region of the distal diaphysis. In the previous load case this increase is seen in the posterior region.

The stress in the overall bone model is distributed much more evenly and the variation along the length of the bone is also minimal, as opposed to strain contour. Here the stress concentration region is shifted to the medial side of the diaphysis.

## 5

## Discussion

### 5.1 Results

The results achieved from the study are in agreement with the conclusions derived by Bögl *et.al.* [3]. From figure 4.3, it is clear that the Recon implant is successful in distributing and reducing the strains subjected to the femoral neck more effectively as compared to the Antegrade implant. This can be attributed to the fact that in Recon locking method, the screws passing through the femur neck and head help provide structural support to the neck. One notices that the value of strain increases from the distal neck region to the proximal neck region. Hence, over an elongated cycle of loading and unloading, it is highly probable that failure is initiated in the proximal region of the neck. It is also important to note that the absolute values of the strains obtained in this study may not necessarily represent the real life scenario, as mentioned earlier, because muscle forces all across the geometry of the bone do provide additional stiffness in keeping the bone in place under application of heavy loads. The strains over the shaft of the bone are mainly distributed towards the distal region of the shaft, with the penetration across the cross section also being higher as compared to the proximal region. This can be attributed to the fact that the resultant moment caused due to the hip load will have the highest value in distal diaphysis, due to it being farther away from the point loading.

The maximum principal stresses (figure 4.4) incurred in the neck region are lower for the Recon implant as compared to the Antegrade implant. The principal stresses are distributed over a larger portion of the side neck in the Antegrade implant when compared to the Recon implant, with the highest values obtained towards the topmost regions of the neck. The highest stresses across the bone geometry are obtained on the outermost cortical surface (where the highest Young's modulus for bone is present) in the shaft, close to the distal locking screws, including the edges of the holes where these screws penetrate the bone surface (stress concentration). A notable difference is that for the loading case with muscle forces, these high stress regions appear in the posterior region of the distal diaphysis (figures 4.9 and 4.10), while they appear medial region of the distal diaphysis (figures 4.14 and 4.15) for loading without muscle forces. The maximum values of stresses (apart from the stress concentration around the nodes on which loads are applied) across the entire bone-implant model, reside along the surface of the implant shaft, and the edges of the holes of the screws in the implant nail/rod. This is understandable, as the implant material has the highest value of young's modulus across the bone-implant model.

From figure 4.11c, it is evident that the region between the two screws in the Recon implant has a higher value of strain than the surrounding regions, which could lead to a risk of peri-implant fractures. However, the strains across the region from lesser trochanter to the greater trochanter seem to be slightly higher and widely spread in the Antegrade implant as compared to the Recon implant. This is because the screws across the neck region are effective in transferring the stresses to the nail of the implant from the hip contact load, as

the rigidity/strength of the these screws is similar to that of the rod. This is also the reason why the average strain in the neck of the bone with Antegrade implant is higher than the bone without implant, as there is a mismatch in the highest rigidity in the neck region and the across the shaft for the Antegrade implant. One could hypothesize that the Antegrade implant is slightly more detrimental to the femoral neck or makes the neck more prone to fracture than a similarly dense bone without implants.

## 5.2 Method

### Image segmentation

It was evident from the surveyed literature that for models of biological structures (organs, bones, muscles), image segmentation produces the most effective results, albeit, factors such as the quality of the scan and the segmentation algorithm used play a major role in determining the accuracy and precision of the final model obtained. The model used in this study was a culmination of automatic and manual segmentation methods. The patient in question has osteoporosis, leading to reduced bone density in the regions of femur head and neck, which can clearly be seen in figure 3.2. Also, the patient had undergone a knee replacement procedure prior to the scans, leading to radiological dispersion towards the distal region of the femur bone in the CT scans. A significant discussion took place on the fact that to reduce the errors that may arise out of manually defining the boundaries, only the top half of the femur could be segmented accurately, as the main focus of this study was the femur neck and effect of the two types of implants in that region. However, the decision was made to invest time in studying these boundary definitions, while also consulting with professionals, to be able to produce a complete and realistic model of the femur bone. This was also done to accurately study the effect of loads that were to be applied later, more importantly where the stresses are incurred for a bone without implants and a bone with implants, under the same loading conditions. The final model segmented from the CT scans was entirely under a single label.

### CAD modelling

The CAD models of the implants were designed in Solidworks, due to modelling flexibility, familiarity with the interface and the ease of use of the assembly module. As is evident from the section 3.2, the catalog for these implants mentions a range of length and diametric dimensions for both the nails and the screws. This is because these factors are very patient specific and are decided based on the judgement of the surgeon and geometric specifications of the bone being operated upon. Also, the CAD models were designed to represent the actual manufactured product as close as possible, but certain design specific features were omitted so as to simplify the meshing process later on. However, the dimensions used were from the standardized values mentioned in the catalog. The placement of these implants was consulted with a surgeon from the orthopaedic department of the hospital. This made the final assembly realistic in terms of relative positioning of the bone and the implant.

### Meshing

One of the most important parts of FEA is the selection and definition of the mesh used. The model obtained from ITK snap was very raw, contained a number of faults that needed to be addressed before the conversion process into a solid (NURBS) structure could be carried out. These faults including distorted elements, dangling edges, isolated elements as a result of automatic segmentation algorithm. These elements were generated due to random voxels having comparable intensities to the bone material in the CT scan. Majority of the bone surface was very crude, due to the fact that voxels are essentially three dimensional cuboidal grids, which portrayed the boundary definitions on the surface of the bone in the form of

pointed vertices and edges. Hence, the first step was to smoothen the outer surface to be able map a mesh with reasonable quantity of elements onto it, without requiring a large amount of computational power. The aforementioned isolated elements also needed to be manually located and removed from the model. To covert the surface mesh into a solid object, the geometry needed to be 'watertight'. This operation was performed in Meshlab [16], which provided a ready-made tool for such a process. The solid conversion and the final mesh operations were carried out in Hypermesh, due to it's vast flexibility in meshing operations. To integrate the implant and bone in a single continuous mesh, a boolean operation was perform to remove the bone material where the implant had been positioned. This was done to ensure continuity in the final mesh for effective flow of information throughout the structure. The mesh elements were then cleared off errors such as failure due to jacobian operators, skewness values, normal orientations etc. The minimum and maximum element sizes were decided based on the trade off between reasonable element quantity, maximizing the capture of surface details and allowable number of nodes on the student version of Abaqus CAE. These constraints, especially the last one, are realistic constraints in academic projects.

### Material modelling

The material of the bone is anisotropic in nature, i.e. the properties vary with direction, and also vary depending on the location with in the bone. However, to replicate such a behavior in it's true sense, the degree and nature of modelling needs to be on a microscopic level, which simply wasn't feasible with available time and resources. Hence, the material was treated as an isotropic material, as was the case in all of the relevant literature that was studied. With in the regions of trabecular bone and cortical bone the material properties vary over a wide range. Initially, when the material mapping strategy was undecided, a set of options were available in terms of the segmentation model. One option was to segment these bone materials separately and export them as separate surfaces. However, this proved to be a tedious task in the meshing stage in terms of stitching the surfaces together/defining appropriate contact behaviour between, while retaining the definitions of separate labels. A mass generalization of the material property would yield unrealistic results, which then prompted rethinking of the material mapping strategy. With Bonemat, a reasonable degree of sophistication was added to the material modelling aspect. The final model created contained over a 1000 different material sets (all but one of which belonged to the bone material, as the implant material had same values of properties throughout), which differed in the value of the Young's modulus assigned to each element of the FE mesh based on their location in their respective intensity region on the CT scan.

### 5.3 Limitations and future scope

In the human body, bones are not held in place by simple mechanical locking mechanisms. The femur is connected with at least 20 different muscle groups all across it's structure as well as at both the hip and the knee joints. These muscles generate forces of their own when ever a hip contact load acts on the femur. The muscle forces are an important part in replicating the actual distribution of stresses and strains, as they do provide additional stiffness in terms of holding the bone in it's place. Hence, eventhough the loads applied in this study represent realistic loads of a gait cycle, the absolute values of the stresses and strains obtained will differ to the real case, as a result of muscle forces.

The segmentation process encompassed almost half of the allotted time for the entire project. This was due a a variety of factors such as an initial lack of knowledge of biological structures from the students, a lack of clearly defined methodology to carry out the process in the existing literature and the complexity of the structure itself. Although, most of these factors were expected due to the multidisciplinary nature of the project. However, this particular process could have been executed more efficiently to conserve the resource of time,

which could be allocated in different areas. In material modelling, however, the limitation is more obvious, which is the fact the bone material is actually anisotropic in nature. Hence, if and when mapping of such properties onto a mesh with thousands of elements becomes a simplified task, the results obtained will certainly be a step closer to replicating the real life scenario even more accurately.

It is also worth mentioning that only a very small percentage of the available literature on the subject described a complete method for the problem tackled in this project. A high percentage of the studies usually neglected one or more key areas of the method that is described in this project. For example, a minimal amount of information was available how the meshing and contact definition for the bone-implant interface was to be modelled, without compromising the continuity of the mesh between the two parts (with entirely different material properties). Such questions are an important part of FEM, and need to be addressed in order to make the analysis realistic.

## 6

## Conclusion

Overall, the aim of this project was to define a methodology that can be replicated - from a CT scan of a bone to a fully functional finite element model of the same bone, obtain realistic behavior on the model and compare the effect of the two implant types on the neck of the femur bone. This was achieved, within the constraints of the available resources. The behavior of the FE model does tend to replicate behavior that is expected under the application of the specific loads, which does validate the material mapping strategy and relative behavior between the bone and the implant. The results obtained confirm the hypothesis that having a nail in the femoral neck produces lesser strain in the neck region compared to the one passing through the lesser trochanter, reducing the risk of fractures in that region. However, outside the scope of this thesis, a lot more data can be derived from these FE models. For example, conducting impact analysis - analyzing the behavior and damage due to falls - which is believed to be a major reason for these femoral fractures, may yield results that can help in backing clinical theories. Since the patient is suffering from osteoporosis, where the bone regeneration or healing capability is impaired, fatigue fracture can also be a cause of concern. Hence, a fatigue analysis of the model may produce improved understanding. Finally, it can be concluded by saying the results are able to answer the research questions within the domain of reasoning.

# I Appendix

For finding the correlation between  $\rho : qct$  and the HU, the HU for the materials in the calibration phantom were initially found. For this, first the pixel intensity values were converted into HU values and then taking its average across the pixels depicting the particular phantom material. The relation between the HU values and the pixel intensity is a linear equation of the form:

$$HU = mx + c \tag{I.1}$$

Where,  $x$  is the pixel intensity value,  $m$  is the slope of the curve and  $c$  is the intercept point. These values are taken from DICOM metadata file where the calibration data for the CT machine is stored. Hence equation (I.1) becomes:

$$HU = x - 1024 \tag{I.2}$$

Converting the image into a 2-D matrix of size equal to the image resolution, where each cell holds the intensity value of the pixel at that position in the image. Using the above equation (I.2) we get a matrix of the HU values. From this it is easy to select the cells that correlate to the pixels depicting a particular phantom material whose HU value is needed (figure I.1).

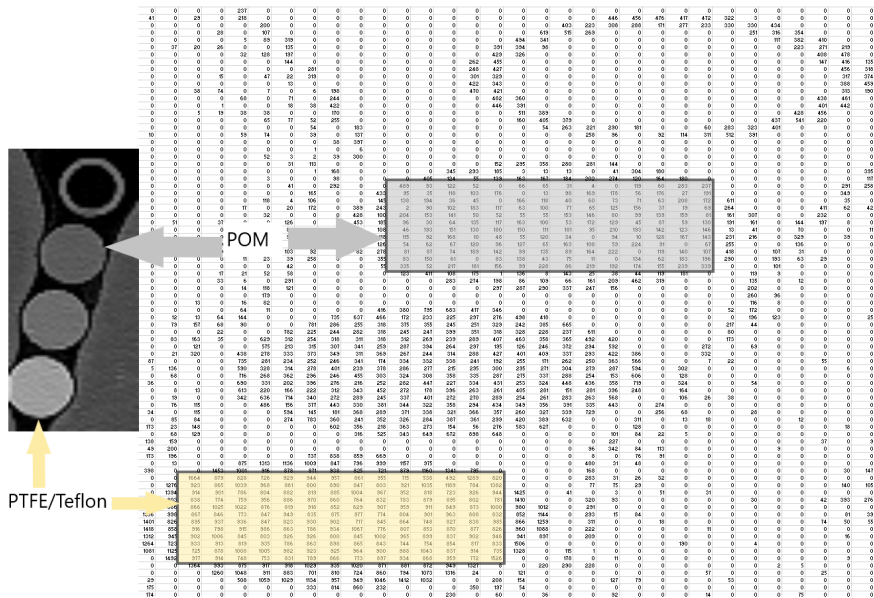


Figure I.1: Image slice used to calculate HU average

The coefficients for equation (3.1) were found using the values of two materials: POM and Teflon, these have been pointed out in the figure I.1 above. Table I.1, below, shows the

---

calculated average HU value for the two materials. These values are in close agreement with the provided values.

Table I.1: Calculated HU values.

Material Name	HU Value	
	Calculated	Provided
Polyoxymethylene (POM)	316.5536	300
Polytetrafluoroethylene (PVDF/Teflon)	890.2308	950

Substituting these values from table I.1 into equation (3.1) we get the coefficients as:

$$a = 1.0002 \quad b = 1.3477 \times 10^{-3}$$



## Bibliography

- [1] Nicola Veronese and Stefania Maggi. “Epidemiology and social costs of hip fracture”. In: *Injury* 49.8 (2018), pp. 1458–1460.
- [2] John A Kanis, Anders Oden, Eugene V McCloskey, Helena Johansson, Denys A Wahl, and Cyrus Cooper. “A systematic review of hip fracture incidence and probability of fracture worldwide”. In: *Osteoporosis international* 23.9 (2012), pp. 2239–2256.
- [3] Hans Peter Bögl, Georg Zdolsek, Karl Michaëlsson, Jonas Höijer, and Jörg Schilcher. “Reduced Risk of Reoperation Using Intramedullary Nailing with Femoral Neck Protection in Low-Energy Femoral Shaft Fractures”. In: *JBJS* 102.17 (2020), pp. 1486–1494.
- [4] *FIN - Femur Intramedullary Nail: Product: Products: Tst Tibbi Aletler San. Ve Tic. Ltd. Sti.* URL: <http://tstsan.com/en/urun/i/179/fin-femur-intramedullary-nail.html>. (accessed: 08.02.2021).
- [5] *Femur Fracture Physiotherapy*. URL: <https://www.phoenixrehabgroup.com/femur-fracture-physiotherapy.html>.
- [6] *WikiJournal of medicine/medical gallery of blausen medical 2014 - wikiversity*. 2021. URL: [https://en.m.wikiversity.org/wiki/WikiJournal\\_of\\_Medicine/Medical\\_gallery\\_of\\_Blausen\\_Medical\\_2014](https://en.m.wikiversity.org/wiki/WikiJournal_of_Medicine/Medical_gallery_of_Blausen_Medical_2014).
- [7] R. Bartl and Christoph Bartl. *Bone disorders : biology, diagnosis, prevention, therapy*. Springer, 2016. ISBN: 9783319291826. URL: <https://login.e.bibl.liu.se/login?url=https://search.ebscohost.com/login.aspx?direct=true&db=cat00115a&AN=1kp.870430&site=eds-live&scope=site>.
- [8] Granta Design Limited, Cambridge, UK. *GRANTA EduPack software*. 2020. URL: [www.grantadesign.com](http://www.grantadesign.com).
- [9] R Bruce Martin, David B Burr, Neil A Sharkey, David P Fyhrie, et al. *Skeletal tissue mechanics*. Vol. 190. Springer, 1998.
- [10] Paul A. Yushkevich, Joseph Piven, Heather Cody Hazlett, Rachel Gimpel Smith, Sean Ho, James C. Gee, and Guido Gerig. “User-guided 3D active contour segmentation of anatomical structures: Significantly improved efficiency and reliability”. In: *NeuroImage* 31.3 (2006), pp. 1116–1128. ISSN: 1053-8119.
- [11] Anil Kalra. “Chapter 9 - Developing FE Human Models From Medical Images”. In: *Basic Finite Element Method as Applied to Injury Biomechanics*. Ed. by King-Hay Yang. Academic Press, 2018, pp. 389–415. ISBN: 978-0-12-809831-8. DOI: <https://doi.org/10.1016/B978-0-12-809831-8.00009-X>. URL: <https://www.sciencedirect.com/science/article/pii/B978012809831800009X>.
- [12] Fulvia Taddei, Enrico Schileo, Benedikt Helgason, Luca Cristofolini, and Marco Viceconti. “The material mapping strategy influences the accuracy of CT-based finite element models of bones: An evaluation against experimental measurements”. In: *Medical Engineering Physics* 29.9 (2007), pp. 973–979. ISSN: 1350-4533. DOI: <https://doi.org/10.1016/j.medengphy.2006.10.014>. URL: <https://www.sciencedirect.com/science/article/pii/S1350453306002293>.

- [13] Tony S Keller. "Predicting the compressive mechanical behavior of bone". In: *Journal of biomechanics* 27.9 (1994), pp. 1159–1168.
- [14] Enrico Schileo, Enrico Dall'Ara, Fulvia Taddei, Andrea Malandrino, Tom Schotkamp, Massimiliano Baleani, and Marco Viceconti. "An accurate estimation of bone density improves the accuracy of subject-specific finite element models". In: *Journal of biomechanics* 41.11 (2008), pp. 2483–2491.
- [15] Benedikt Helgason, Egon Perilli, Enrico Schileo, Fulvia Taddei, Sigurður Brynjólfsson, and Marco Viceconti. "Mathematical relationships between bone density and mechanical properties: a literature review". In: *Clinical biomechanics* 23.2 (2008), pp. 135–146.
- [16] Paolo Cignoni, Marco Callieri, Massimiliano Corsini, Matteo Dellepiane, Fabio Ganovelli, and Guido Ranzuglia. "MeshLab: an Open-Source Mesh Processing Tool". In: *Eurographics Italian Chapter Conference*. Ed. by Vittorio Scarano, Rosario De Chiara, and Ugo Erra. The Eurographics Association, 2008. ISBN: 978-3-905673-68-5. DOI: 10.2312/LocalChapterEvents/ItalChap/ItalianChapConf2008/129-136.
- [17] *Defining MPC Constraints*. 2021. URL: <https://abaqus-docs.mit.edu/2017/English/SIMACAECAERefMap/simacae-t-itnhelptopicmultipoint.htm>.
- [18] Georg Bergmann, Alwina Bender, Jörn Dymke, Georg Duda, and Philipp Damm. "Standardized loads acting in hip implants". In: *PloS one* 11.5 (2016), e0155612.
- [19] ME Taylor, KE Tanner, MAR Freeman, and AL Yettram. "Stress and strain distribution within the intact femur: compression or bending?" In: *Medical engineering & physics* 18.2 (1996), pp. 122–131.
- [20] Anna Gustafsson, Jörg Schilcher, Lorenzo Grassi, Per Aspenberg, and Hanna Isaksson. "Strains caused by daily loading might be responsible for delayed healing of an incomplete atypical femoral fracture". In: *Bone* 88 (2016), pp. 125–130.